Non-Invasive In Vivo Ultrasound Temperature Estimation

A DISSERTATION
SUBMITTED TO THE FACULTY OF THE GRADUATE SCHOOL
OF THE UNIVERSITY OF MINNESOTA
BY

Mahdi Bayat

IN PARTIAL FULFILLMENT OF THE REQUIREMENTS
FOR THE DEGREE OF
Doctor of Philosophy

Emad S. Ebbini, Adviser

June, 2014

Acknowledgements

I am grateful for the support of many individuals who have helped make this research possible. I would especially like to express my highest gratitude to my adviser, Prof. Emad Ebbini, who was not only an excellent mentor but a great friend who will continue to impact my professional life. It was his great way of thinking and timely feedback that made this research possible. I am grateful to the members of my committee: Prof. James Leger, Prof. Mostafa Kaveh and Prof. John Bischof for reviewing my dissertation and providing insightful and invaluable comments. I would like to extend my special thanks to Dr. John Ballard, a great friend whom I was fortunate to work with and share many ideas during discussions and brainstorming. I would also like to appreciate him for reviewing my dissertation and providing helpful comments. I would like to thank Dr. Dalong Liu whose exceptional talent and work in integrating the imaging and therapy system was the fundamental asset in the ultrasound imaging and signal processing lab and it will be of great value for all researchers at the lab for years to come. I would like to thank Mr. Elias Wilken-Resman whose OpenCL code for speckle tracking displacement estimation code was a perfect acceleration in pre-assessment of many experimental data sets. I would also like to thank Ms. Alyona Haritonova for her help during experiments and data collections. I would also like to thank other current and past members of the UISPL for their help and kind friendship throughout this research.

Last but not least, I would like to thank my family for being the continuous source of support and motivation during the hardest and most strenuous life experiences. I would especially like to thank my brother, Reza, whose sacrifice and dedication to my progress has been beyond extraordinary. I would like to thank my wife, Shabnam, whom I share the best moments of my life and her unconditional support has been with me from the very first moment we met.

Dedication

To my family

Abstract

New emerging technologies in thermal therapy require precise monitoring and control of the delivered thermal dose in a variety of situations. The therapeutic temperature changes in target tissues range from few degrees for releasing chemotherapy drugs encapsulated in the thermosensitive liposomes to boiling temperatures in complete ablation of tumors via cell necrosis. High intensity focused ultrasound (HIFU) has emerged as a promising modality for noninvasive surgery due to its ability to create precise mechanical and thermal effects at the target without affecting surrounding tissues. An essential element in all these procedures, however, is accurate estimation of the target tissue temperature during the procedure to ensure its safety and efficacy.

The advent of diagnostic imaging tools for guidance of thermal therapy was a key factor in the clinical acceptance of these minimally invasive or noninvasive methods. More recently, ultrasound and magnetic resonance (MR) thermography techniques have been proposed for guidance, monitoring, and control of noninvasive thermal therapies. MR thermography has shown acceptable sensitivity and accuracy in imaging temperature change and it is currently FDA-approved on clinical HIFU units. However, it suffers from limitations like cost of integration with ultrasound therapy system and slow rate of imaging for real time guidance. Ultrasound, on the other hand, has the advantage of real time imaging and ease of integration with the therapy system. An infinitesimal model for imaging temperature change using pulse-echo ultrasound has been demonstrated, including *in vivo* small-animal imaging. However, this model suffers from limitations that prevent demonstration in more clinically-relevant settings. One limitation stems from the infinitesimal nature of the model, which results in spatial inconsistencies of the estimated temperature field. Another limitation is the sensitivity to tissue motion and deformation during *in vivo*, which could result in significant artifacts.

The first part of this thesis addresses the first limitation by introducing the Recursive Echo Strain Filter (RESF) as a new temperature reconstruction model which largely corrects for the spatial inconsistencies resulting from the infinitesimal model. The performance of this model is validated using the data collected during subtherapeutic temperature changes in the tissue mimicking phantom as well as *ex vivo* tissue blocks.

The second part of this thesis deals with *in vivo* ultrasound thermography. Tissue deformations caused by natural motions (e.g. respiration, gasping, blood pulsation etc) can create non-thermal changes to the ultrasound echoes which are not accounted for in the derivation of physical model for temperature estimation. These fluctuations can create severe artifacts in the estimated temperature field. Using statistical signal processing techniques an adaptive method is presented which takes advantage of the localized and global availability of these interference patterns and use this data to enhance the estimated temperature in the region of interest. We then propose a model based technique for continuous tracking of temperature in the presence of natural motion and deformation. The method uses the direct discretization of the transient bioheat equation to derive a state space model of temperature change. This model is then used to build a linear estimator based on the Kalman filtering capable of robust estimation of temperature change in the presence of tissue motion and deformation. The robustness of the adaptive and model-based models in removing motion and deformation artifacts is demonstrated using data from *in vivo* experiments. Both methods are shown to provide effective cancellation of the artifacts with minimal effect on the expected temperature dynamics.

Contents

List of Figures

Chapter 1

Introduction

1.1 Thermal Therapy

Thermal therapy is a treatment method which dates back to the earliest practice of medicine. Increasing and decreasing temperature in different parts of the body has been used for treatment of diseases including cancer. Recent researches have shown the impact of the thermal stress on the functionality of the biological cells. Tumor tissue destruction due to ablation [4], palliation of painful bone metastases [5], treatment of uterine fibroid [6] and cardiac ablation for treatment of atrial fibrillation [7] are examples of the modern applications of thermal therapy. Localized drug delivery is another important application which is becoming an alternative method for chemotherapy. Thermal and mechanical effects of the ultrasound beam can release the chemotherapy drugs such as Doxorubicin, encapsulated in the temperature sensitive shells, very close to the target organ without affecting other parts of the body [8]. Among other thermal treatments, non-invasive or minimally invasive methods have become more attractive due to ease of operation and reduction in the patient's post treatment discomfort. Most of these operations can be performed as outpatient treatment with minimal complications and discomfort. For example, women undergoing magnetic resonance guided focused ultrasound (MRgFUS) surgery in uterine fibroid were able to go back to work after an average time of 1 day. This time is 13 days for Uterine Artery Embolization (UAE) and 6 weeks for abdominal myomectomy [9]. A schematic of the treatment setup is shown in Fig. (1.1).

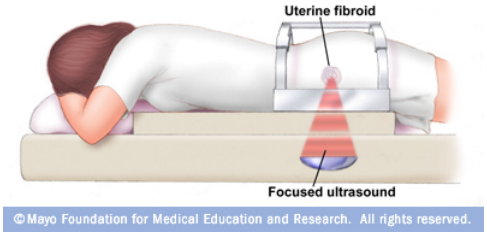

Figure 1.1: Ablation of uterine fibroid using magnetic resonance guided focused ultrasound. Image taken from mayoclinic.org, Mayo foundation.

Thermal therapies involving cell necrosis can be performed in two different ways. In one approach, a rapid temperature change up to $80°C$ and above is created to develop coagulation and cell necrosis through protein denaturation [10]. Another group of treatments, called hyperthermia, include slow heating of the tissue such that a temperature of $43°C$ is maintained for a few minutes. The equation that governs the required thermal dose for the efficacy of the treatment is based on the Arrhenius damage integral [11].

The success and efficacy of all thermal therapies depend upon a controlled and localized heat creation, monitoring and control mechanism that spares the tissues surrounding the target region for therapy. There are many ways to create such a controlled and spatially confined heating pattern. Microwave, radiofrequency, laser and ultrasound are the most common modalities used for creating non-invasive or minimally invasive controlled heating patterns among which ultrasound has gained more attraction due its versatility, safety and deep penetration [12]. With recent advances in piezocomposite technology, arrays of small elements are fabricated which can be individually excited. This feature enables optimal beamforming at the transmit and receive sides with applications both in therapy and imaging. The ability to focus and steer the ultrasound beam deep into tissue plays an essential role in High Intensity Focused Ultrasound (HIFU) for delivery of high dose of acoustic energy at specific locations without having significant impact on the surrounding tissue. A natural requirement for all thermal therapies, however, is guidance and control of the energy dose to assure the effectiveness of the procedure and at the same time providing safety to the surrounding areas and this has been a topic of research as early as the thermal therapy was conceived. Both invasive and non-invasive

techniques have been used for temperature estimation and control. In invasive techniques a thermocouple is inserted into the area where the thermal energy is delivered. In radiofrequency and microwave ablation techniques which use a needle antenna to deliver the energy, a thermocouple is also included to record the simultaneous temperature change. The temperature mapping, however, is limited to a single point corresponding to the thermocouple junction. Non-invasive methods use an imaging modality which shows sensitivity to the temperature. Ultrasound and Magnetic Resonance (MR) are two imaging modalities with acceptable sensitivity to the temperature.

1.2 Magnetic Resonance Temperature Estimation

Magnetic resonance is an attractive imaging technique with superior spatial resolution and safety due to lack of ionizing radiation and non-invasive nature. There are several parameters in MR which show temperature sensitivity.

1.2.1 Proton Density

Proton density is proportional to the equilibrium magnetization which in turn is inversely proportional to the temperature and changes $-0.3 + 0.01\%/^{\circ}C$ between 37° C and 80° C [13]. This range of variations requires a high signal to noise ratio and long repetition times in the order of 10 seconds [14] which make this method impractical for real time applications with rapid temperature changes.

1.2.2 T_1 Relaxation Time of Water Protons

Translational and rotational motions of the biological elements create dipolar interactions between biological macromolecules and water molecules. This process controls the spine-lattice relaxation time, T_1, in the magnetically excited tissue [15]. This time is an increasing function of temperature and can be used as a parameter to track temperature changes. The parameters relating the change of temperature to the relaxation time are tissue dependent and tissue heterogeneity can deteriorate the performance of temperature estimation. This degradation is more pronounced in the tissue with large fat content due to large differences in T_1. Accurate tracking of T_1 requires long mapping process (in order of minutes) which renders this method less attractive for fast tracking

of temperature changes and more suitable for qualitative assessment of temperature distribution [14].

1.2.3 T_2 Relaxation Time of Water Protons

Similar to T_1, spine-spine relaxation time, T_2, can also be used for temperature estimation as it increases with temperature in water. In tissue, however, these changes are not very pronounced and they show nonlinearity to high temperatures [16].

1.2.4 Proton Resonance Frequency

The temperature dependency of the water proton resonance frequency was first reported in [17] and its application in MR thermometry was first addressed in [18]. This method has become the most acceptable modality for MR thermography [19] with superior temperature sensitivity and linearity in a wide range of temperature changes and less dependency on the tissue content. This method can provide temperature estimates with $1^{\circ}C$ standard deviation, 1 second time resolution and around 2 mm spatial resolution [19]. However, changes in susceptibility due to motion can limit the accuracy of this thermometry modality.

1.2.5 Methods Based on other MR parameters

Methods which are based on other parameters such as diffusion coefficients and magnetization transfer have also been developed but they show limited sensitivity and resolution [20],[21] .

In spite of some limitations, results reported in [22],[23],[24] and similar literature show successful implementation of MR for temperature imaging. However, in addition to the sensitivity to motion artifacts and degradation of temperature estimation in the fatty tissues, cost, slow response and the requirements for extra hardware for integration with therapy system are still the main shortcomings of all MR-based thermometry techniques.

1.3 Ultrasound Temperature Estimation

Ultrasound has become increasingly attractive for temperature estimation due to its versatility, low cost and ease of integration with currently available diagnostic machines and HIFU-based therapy systems. The dependency of the back scattered echoes on the temperature is the fact that enables ultrasound to be used for temperature estimation. In the following, ultrasound temperature estimation methods based on different temperature dependent parameters are reviewed.

1.3.1 Mean Speckle Spacing

This method is based on the spectral tracking of the harmonics of the ultrasound echos. Given a regular and limited region of the tissue undergoing temperature changes it is shown that the displacement of the spectral peaks can be related to the change in temperature [25]

$$\Delta f_k(T) \approx \Lambda \Delta T \tag{1.1}$$

where T is the baseline temperature, ΔT temperature change, $\Delta f_k(T)$ is the frequency shift of the k^{th} harmonic and Λ is a constant defined by the local tissue properties. High resolution spectral estimation methods such as one presented in [26] can be used to accurately track the harmonic shifts and be linearly mapped to the temperature. The performance of this method, however, depends upon existence of uniform scatterers region. Specular reflectors and inhomogeneity in the underlying tissue can adversely affect the temperature estimation accuracy [26].

1.3.2 Variations in Attenuation Coefficients

The feasibility of using ultrasound attenuation for temperature estimation was first studied in [27]. A temperature error of 20% was reported for temperature rise of about 10°C in a phantom. Several other groups observed that a better relationship between attenuation and temperature change can be found at 50°C and higher [28],[29],[30]. The work in [31] investigated the dependency of the ultrasound attenuation on a range of $25° - 95°$ C in tissue samples. They found that significant changes in ultrasound start after 60° C. Other groups [32], [33] also reported similar result indicating that ultrasound temperature estimation using attenuation coefficients is more attractive for

high temperature changes and shows poor performance for monitoring hyperthermia (a temperature change of about 10° C)[34]. No specifications about temporal and spatial resolution of this meths have been reported.

1.3.3 Change in Backscattered Energy

Based on the temperature dependency of the backscattered power presented in [35], authors in [36] showed that the relative backscattered power normalized to baseline temperature backscattered power shows monotonic increase or decrease with temperature change in the hyperthermia range (up to 50° C). This method showed a sensitivity of around 0.38 dB/$^{\circ}C$. The direction of backscattered power changes was determined by the tissue content such that experiments in lipid showed 5 dB increase while experiments in aqueous showed a 3 dB decay in the backscattered power at 50°C compared to the backscattered power at 37°C. They showed that effect of attenuation can be neglected in the hyperthermia range. The subsequent results presented in [34] and [37] confirmed the results in different tissue samples and in *in vivo* respectively. However, these methods show poor spatial resolution in the order of 1 cm^3 and they seem to perform well in slow heating scenarios where a temperature change of 10 to 13° C occurs during several minutes leading to a poor temporal resolution.

1.3.4 Ultrasound Echo Shifts

Local temperature changes create echo shifts due to physical and apparent displacements. The former is the result of thermal expansion while the rather is related to the local changes in speed of sound. Using an infinitesimal model for thermal expansion and a linear temperature dependency assumption for the speed of sound, Simon *et al.* [38] suggested a model that lumped these two effects in a single equation which related the echo strain to the induced temperature change. We call this the infinitesimal echo strain filter or δ-ESF model. Similar results were reported in [39] where the requirement for a good thermal expansion model was also explained. Based on the δ-ESF model and using the speckle tracking method explained in [38], authors in [40] demonstrated the real-time tracking of the temperature change *in vivo* using the integrated imaging-therapy system described in [41]. This model has also been confirmed

by other groups [42],[43] and [44] where some limitations have been addressed as well as solutions for some of the common problems such as the thermoacoustic lens effect have been suggested [45]. In spite of successful implementation of δ-ESF model, ignoring nonuniform baseline temperature and directionality of the thermal expansion can lead to unrealistic temperature fluctuations inconsistent with the physics of the temperature spatio-temporal distribution. Nevertheless, the echo shift based ultrasound temperature estimation methods show excellent spatial and temporal resolution when implemented using sub-sample accuracy speckle tracking algorithms and at high frame rate imaging.

1.4 *In Vivo* Ultrasound Temperature Estimation and Natural Motion Artifacts

Another major challenge in monitoring temperature using ultrasound is the interference and artifacts due to natural motions of the patient. Theses motions can include respiration, gasping, blood pulsation or simply patient movement. The assumption, however, is that these movements do not change the distributions of the ultrasound speckles significantly and the displacement is mainly within the dynamic range of the speckle tracking algorithm. This assumption is fairly valid as long as imaging is performed at relatively high frame rates.

Natural motions cause deformation in the underlying tissue which in turn creates strain patterns in the echo displacement field. When a blood vessel pulsates, the wall movement acts as a vibrating membrane which propagates the pressure field throughout the the entire surrounding tissues. These patterns interfere with the temperature induced echo strain data calculated by the speckle tracking algorithm. In contrast to the echo strain due to temperature, however, the deformation patterns tend to have different statistical, spatial, temporal and spectral properties which make it possible to deal with using appropriate signal processing techniques.

In [46] a method for separating the motion displacement from temperature is presented which is based on different window sizes in speckle tracking in case of translational motion and deformation in a rubber phantom. Another correlation-based method is presented in [47] in which incremental displacement frames are selected based on a cross correlation similarity with the last selected frame in a region of interest outside

the heated volume. Motions that create large decorrelations can be avoided using this method. However, these methods are not applicable for tracking of fast temperature changes with high frame rate speckle tracking. The results presented in [40] and [48] show that post processing of the temperature using a two dimensional filter inspired by the bioheat equation can further reduce some of the inconsistencies including the ripples caused by the thermal lens effect and sudden transitions due to mechanical stresses. However due to shared bandwidth of the artifacts and the temperature field, a filtering mechanism with spatial and temporal selectivity is preferred.

1.5 Contribution of this Dissertation

1.5.1 A New Model for Echo Shift-Based Ultrasound Thermography

In the first part of this thesis, we investigate a new way of modeling the ultrasound echo changes due to the thermal excitation. In this regard a new formulation of the temperature change based on displacements in the back scattered echoes is presented which allows for including the directionality of the thermal expansion and nonuniform baseline temperature. The results of this model are shown to provide more consistent spatio-temporal distribution of the temperature with respect to the bioheat equation. The new model is called Recursive Echo Strain Filter (RESF) due to its infinite impulse response digital filter realization. The parameters of this filter are shown to be tissue dependent and by using an effective recursion length parameter, the RESF model can change to the δ-ESF model. The accuracy and repeatability of the RESF model is verified by applying it to multiple data sets and thermocouple readings.

1.5.2 Ray Tracing Modeling of the Ultrasound Beam Aberration

We present a ray tracing modeling of the ultrasound beam propagation to evaluate the extent of the aberration caused by temperature heterogeneity. A variational calculus technique is used to calculate the ray trajectory passing through a heterogeneous speed of sound medium based on the Fermat's least time principle. The simulation results provide a qualitative validation of the thermal lens effect seen during echo shift based

ultrasound thermography.

1.5.3 Adaptive and Model Based Techniques for *in vivo* Ultrasound Temperature Estimation

In the second part of the dissertation we present adaptive and model based techniques for *in vivo* ultrasound temperature estimation. We first present a motion compensation technique which is based on the global availability of the motion artifact. The method uses deformation information outside the target region to compensate within the temperature tracking region. Then, we present a model based technique for ultrasound temperature estimation. The dynamic model of the temperature change is derived by direct discretization of the bioheat equation. A Kalman filter approach is presented where by using pure prediction cycles continuous tracking of temperature changes during *in vivo* natural motions becomes possible without further information.

1.6 Organization of the Dissertation

This dissertation is organized as follows. An overview of thermal therapy and monitoring techniques was presented in chapter 1. In chapter 2 we address the problem of modeling temperature estimation using displacement in the ultrasound echoes computed by speckle tracking method. The RESF model is presented which accounts for nonuniform baseline temperature. Chapter 3 provides the phantom and *in vitro* results and comparison between δ-ESF and RESF models. A ray tracing modeling based on variational solution of the Fermat's least time principle is presented in chapter 4 where we discuss the extent of the beam aberration when passing through a highly focused temperature change field. Chapter 5 covers the adaptive and model based techniques for *in vivo* ultrasound temperature estimation. Chapter 6 provides the *in vivo* results with a discussion of the achievements. Chapter 7 concludes this dissertation with a summary of the work and possible future extensions of the research.

Chapter 2

Temperature Estimation Models Based on Ultrasound Echo Shifts

2.1 Introduction

Localized temperature changes create shifts in the ultrasound backscattered echoes. These displacements include physical shifts due to thermal expansions and apparent shifts due to change in speed of sound. We first describe the model presented in [38] for ultrasound temperature estimation. We call this model the Infinitesimal Echo Strain Filter (δ-ESF) model. We then present the Recursive Echo Strain Filter (RESF) model that addresses some of the limitations of the δ-ESF model

2.2 Infinitesiml Echo Strain Filter (δ-ESF) model

The delay from a scattering point located at depth z and baseline temperature θ can be written as

$$\tau(z;\theta) = 2\int_0^z \frac{d\xi}{c(\xi;\theta)} \tag{2.1}$$

where is c is the local speed of sound and it is a function of temperature and depth in general. The echo shift due to a small increase in temperature can then be written as [38]

$$\delta\tau(z,T) = 2\int_0^z \frac{d\xi(\theta+\delta\theta)}{c(\xi;\theta+\delta\theta)} - 2\int_0^z \frac{d\xi}{c(\xi;\theta)} \tag{2.2}$$

where T is the frame (wall clock) time. The first term in the right hand side of the (2.2) reflects the changes in echo via change in local speed of sound as well as infinitesimal changes in the spatial element due to thermal expansion. Assuming a linear model for the change in speed of sound and thermal expansion

$$c(\xi;\theta+\delta\theta) = c(\xi;\theta)(1+\beta\delta\theta) \tag{2.3}$$

$$d\xi(\theta+\delta\theta) = d\xi(\theta)(1+\alpha\delta\theta) \tag{2.4}$$

where $\beta = \frac{1}{c}\frac{dc}{d\theta}$ and $\alpha = \frac{1}{L}\frac{dL}{d\theta}$ are the linear speed of sound and thermal expansion coefficients respectively. Plugging (2.3) and (2.4) in (2.2 and using first order approximations we have

$$\delta\theta = \frac{c}{2}\frac{1}{(\alpha-\beta)}\frac{\partial\delta\tau(z)}{\partial z} \tag{2.5}$$

Using the fact that $d\tau = 2dz/c$ and introducing t as the variable along the delay axis

$$\delta\theta = \frac{1}{(\alpha-\beta)}\frac{\partial\delta\tau(z)}{\partial t} \tag{2.6}$$

where the small temperature change is directly related to the echo strain via thermal coefficients. This model suggest a differentiator along the axial direction which has a very simple realization. However, to limit out of band noise the differentiator can be followed by a low-pass filter with a cutoff frequency that preserves the temperature spatial frequencies. In addition to the noise, this model is very sensitive to the aberrations caused by thermal lens effect [38]. The latter especially, can create ripples at and beyond the heated region deteriorating the specificity of the estimated temperature profile. To limit the adverse effects of noise and thermal lens, a spatial FIR low-pass filter was proposed in [38] to limit the effective bandwidth of the differentiator implied by (2.6). The parameters of this post filtering step, however, were defined experimentally based on the axial-lateral extent of the power deposition and it was emphasized that this ad hoc filtering degrades the spatial resolution as well as the quantitative accuracy of the estimated temperature. In the next section we introduce a new model where instead of considering the infinitesimal changes in the thermal expansion, the cumulative changes are included in the derivation. This change in the model results in a band limited differentiator in which the parameters are defined based on the tissue properties. Another

shortcoming of the δ-ESF model is ignoring the possible directionality of the thermal expansions. As in case of HIFU, where the thermal dose is delivered through a highly localized temperature change, thermal expansion causes the scatterers to move away from the center of heating creating a directional displacement in the echos. Using the model in (2.2) for the echo shifts, it is not possible to account for such directionality.

2.3 Recursive Escho Strain Filter (RESF) Model

When using a highly localized heating source like HIFU, it might be a valid assumption that thermal stress causes the points to move away from the center of heating. This effect causes the points between the transducer and the focus to move toward the transducer while points behind the focus are pushed away from the transducer. The δ-ESF model is not able to account for such directionality. Using the delay equation in (2.1), for any point between the transducer and heating center located at depth z and baseline temperature of θ, the echo shift can be written as

$$\delta\tau(z;\theta) = 2\int_0^{z(\theta+\Delta\theta)} \frac{d\xi}{c(\xi;\theta+\Delta\theta)} - 2\int_0^{z} \frac{d\xi}{c(\xi;\theta)} \tag{2.7}$$

where $\Delta\theta$ is the differential change in temperature at depth z. Using the linear thermal coefficients defined in (2.3) and (2.4) we have

$$\delta\tau(z,T) = 2\int_0^{z(\theta)(1-\alpha\Delta\theta)} \frac{(1-\beta\Delta\theta)d\xi}{c(\xi;\theta)} - 2\int_0^{z} \frac{d\xi}{c(\xi;\theta)} \tag{2.8}$$

and it follows that

$$\delta\tau(z,T) = -2\frac{\alpha z\Delta\theta}{c(z;\theta)} - 2\frac{\alpha\beta z\Delta\theta^2}{c(z;\theta)} - 2\int_0^{z(\theta)} \frac{\beta\Delta\theta d\xi}{c(\xi;\theta)} \tag{2.9}$$

Ignoring the second order terms, this can be further simplified as

$$\delta\tau(z,T) = -2\frac{\alpha z\Delta\theta}{c(z;\theta)} - 2\int_0^{z(\theta)} \frac{\beta\Delta\theta d\xi}{c(\xi;\theta)} \tag{2.10}$$

In the following subsection, using equation (2.10), we show how a closed form solution for the temperature change can be derived which accounts for the change in speed of sound as well. Although the final solution is interesting in terms of the reconstruction model in the spatial domain and it corroborates with a simpler model which follows, the

implementation requires nonuniform sampling transformation and successive updating of speed of sound and temperature field in an iterative fashion. A simpler model can be derived by assuming small variations in the speed of sound and differentiating both sides of the equation (2.10) with respect to z

$$\frac{\partial \delta\tau(z,T)}{\partial z} = -2\frac{\alpha\Delta\theta}{c(z;\theta)} - 2\frac{\alpha z \partial\Delta\theta/\partial z}{c(z;\theta)} - 2\frac{\beta\Delta\theta}{c(z;\theta)} \tag{2.11}$$

substituting for ∂z by $c\partial t/2$ in (2.11) results in the following simplified equation

$$\frac{\partial \delta\tau(z)}{\partial t} = -(\alpha+\beta)\Delta\theta - \alpha\frac{z}{c}\frac{\partial\Delta\theta}{\partial t} \tag{2.12}$$

where t is the time variable along the delay axis based on (2.1). In general, equation (2.12) is a nonlinear differential equation which can be solved numerically. However for complexity reasons we would like to form a simpler implementation of the algorithm using only ordinary digital filters. For this reason the depth variable z is replaced by a constant depth z_0. By taking Fourier transform from both sides of the equation (2.12) with respect to the variable t and rearranging the terms

$$\hat{\Delta\theta} = \frac{-j\omega\frac{1}{(\alpha+\beta)}}{1+j\omega\frac{\alpha\tau/2}{(\alpha+\beta)}}\hat{\delta\tau} \tag{2.13}$$

where $\hat{\Delta\theta}$ and $\hat{\delta\tau}$ are the Fourier transforms of $\Delta\theta$ and $\delta\tau$ respectively and we defined $\tau = 2z_0/c$. Equation (2.13) has the form of a differentiator-integrator which can be implemented as an IIR filter in the axial direction or can be combined with time accumulation to form a spatial-temporal filter. It is interesting to note that, at low frequencies, the filter behaves like a differentiator, which is consistent with our earlier model for the infinitesimal temperature change with a constant baseline. The slope of the differentiator is determined by α and β as was shown previously. At higher frequencies, however, the filter has a flat response with a gain of $2/\alpha\tau$. The cutoff frequency of the filter is also a function of the thermal coefficients of thermal expansion and the speed of sound. This result is still attractive from the real-time implementation point of view. Even though the derivation accounted for the inhomogeneous baseline, the final result does not relay on explicit knowledge of this baseline.

The discrete time equivalent of the reconstruction filter in (2.13) can be derived by using the bilinear transformation [49],[50]

$$s = \frac{2}{T}\frac{z-1}{z+1} \tag{2.14}$$

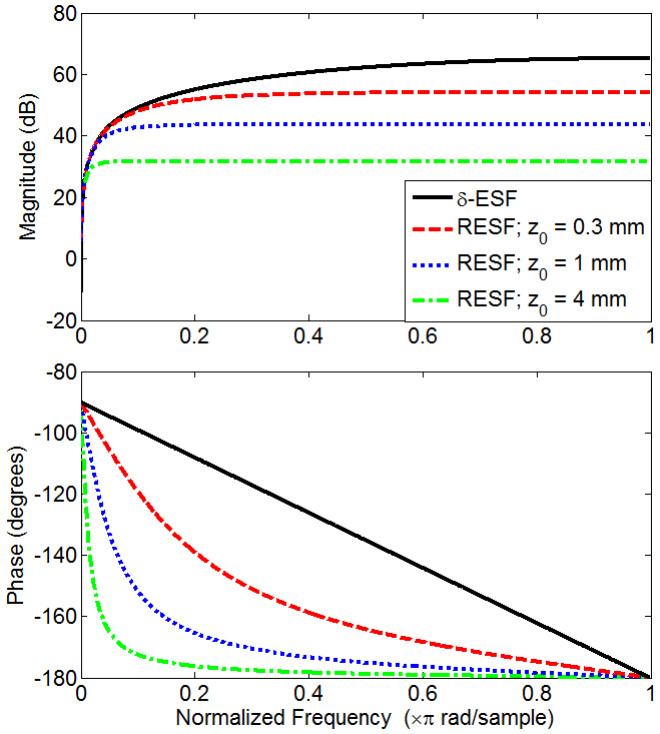

Figure 2.1: Frequency response of the RESF for different depths along with the δ-ESF response for $\alpha = 10^{-4}$ and $\beta = 10^{-3}$. Solid black: the δ-ESF model, dashed red: RESF model with z_0= 0.3 mm, dotted blue: RESF model with z_0= 1 mm and dash-dotted green: RESF model with z_0= 4 mm.

where T is the sampling time or frames rate in our case. Hence

$$\check{\Delta\theta} = \frac{-2T}{T(\alpha+\beta)+\alpha\tau} \frac{1-z^{-1}}{1-\frac{T(\alpha+\beta)-\alpha\tau}{T(\alpha+\beta)+\alpha\tau}z^{-1}} \check{\delta\tau} \tag{2.15}$$

where $\check{\Delta\theta}$ and $\check{\delta\tau}$ are the z transforms of $\Delta\theta$ and $\delta\tau$ respectively.

Equation (2.15) resembles an IIR filter in the axial direction on the displacement data, the main reason that we call this the RESF model. The gain and location of the pole of this filter are defined by α, β (tissue dependent) and $\tau = 2z_0/c$ in which z_0 is the effective length over which the recursion implied by (2.15) occurs. A very small z_0 results in a model that approaches the δ-ESF model.

Fig. (2.1) shows the frequency response of the reconstruction filters based on the δ-ESF model and the RESF model with different z_0 values where we used $\alpha = 1 \times 10^{-4}\ ^\circ\mathrm{C}^{-1}$ and $\beta = 1 \times 10^{-3}\ ^\circ\mathrm{C}^{-1}$. As it can be seen from the plots, as z_0 approaches

zero, the RESF model approaches the δ-ESF model.

For given values of α and β, the effective recursion length, z_0, defines the amount of smoothing implied by the integrator part in (2.15). In monitoring of hyperthermia using HIFU, for example, z_0 can be in the order of the extent of the therapy beam in the imaging plane; typically in the millimeter range.

2.3.1 Closed-Form Solution

At high frame rates where the change in temperature is very small, equation (2.10) becomes

$$d\tau(z,T) = -\frac{2z\alpha d\theta}{c(z;\theta)} - 2\int_0^z \frac{\beta d\theta}{c(\xi;\theta)} d\xi \tag{2.16}$$

where the temperature field $\theta(z,T)$ is considered as a two dimensional function and variable T represents the time progress along M2D frames. The first term in the right hand side of (2.16) represents the change in echo shifts due to the thermal expansion while the second term represents the variations due to the change in speed of sound. By replacing $c(z;\theta)$ with $c(z,T)$ and noticing that the differential in (2.16) is due to time progress we have

$$\frac{\partial\tau(z,T)}{\partial T} = -\frac{2z\alpha}{c(z,T)}\frac{\partial\theta(z,T)}{\partial T} - 2\int_0^z \frac{\beta(\xi,T)}{c(\xi,T)}\frac{\partial\theta(\xi,T)}{\partial T} d\xi \tag{2.17}$$

The time derivative of the echo location in (2.17) can be regarded as the incremental displacement in the speckle tracking algorithm as explained in [38]. Given that the variations of speed of sound with temperature is known, in its general form, equation (2.17) represents a non-homogeneous nonlinear integro-differential equation of temperature distribution over time and space. A consistent solution for this equation should satisfy the bio-heat equation with given boundary and initial conditions. Taking Fourier transform from both sides of (2.17) with respect to variable z

$$\begin{aligned}\mathcal{F}_z\left\{\frac{\partial\tau(z,T)}{\partial T}\right\} = -2\alpha j\frac{d}{dk_z}\mathcal{F}_z\left\{\frac{1}{c(z,T)}\frac{\partial\theta(z,T)}{\partial T}\right\} - \\ \frac{2}{jk_z}\mathcal{F}_z\left\{\frac{\beta(z,T)}{c(z,T)}\frac{\partial\theta(z,T)}{\partial T}\right\}\end{aligned} \tag{2.18}$$

Considering β as a constant and defining $\varphi = (\partial\theta/\partial T)/c$ we have

$$\mathcal{F}_z\left\{\frac{\partial\tau(z,T)}{\partial T}\right\} = -2\alpha j\frac{d\phi}{dk_z} - \frac{2}{jk_z}\beta\phi \tag{2.19}$$

where $\phi = \mathcal{F}_z\{\varphi\}$. Alternatively

$$\frac{d\phi}{dk_z} - \frac{\beta}{\alpha}\frac{\phi}{k_z} = -\frac{1}{2\alpha j}\mathcal{F}_z\left\{\frac{\partial\tau(z,T)}{\partial T}\right\} \tag{2.20}$$

Equation (2.20) is a solvable ordinary differential equation (ODE) with respect to variable k_z with the following closed form solution

$$\phi = -k_z^{\beta/\alpha}\int\frac{k_z^{-\beta/\alpha}}{2\alpha j}\mathcal{F}_z\left\{\frac{\partial\tau(z,T)}{\partial T}\right\}dk_z \tag{2.21}$$

and taking inverse Fourier transform

$$\varphi = -\mathcal{F}_z^{-1}\left\{k_z^{\beta/\alpha}\int\frac{k_z^{-\beta/\alpha}}{2\alpha j}\mathcal{F}_z\left\{\frac{\partial\tau(z,T)}{\partial T}\right\}dk_z\right\} \tag{2.22}$$

The last equation relates the temperature rate to the incremental displacement via baseline speed of sound which can be in turn updated sequentially. Considering that equation (2.22) is derived with minor assumptions about change in speed of sound and temperature heterogeneity, it still resembles the form of a differentiator-integrator suggested by (2.13) with appropriate assumptions about α and β.

2.3.2 Bi-directional thermal expansion

The reconstruction filter implied by (2.15) was derived based on the assumption that scatterers move towards the transducer due to thermal expansion. While this is the case for points between the transducer and the center of the heating, it might not valid be for points behind the focus and ideally one would use a different filter for points behind the focus. Any assumption about changing the direction of the thermal expansion, however, would require the knowledge about the point that such change occurs. This information, however, is not available prior to the estimation. Even if such information was available, simply changing the sign of α in equations (2.16) or (2.22) would render the corresponding filter unstable as the pole would be on the right hand side of the complex plane (or outside the unit circle for the case of discrete-time filter). This is

due the fact that these filters are derived based on some approximations not completely valid for the entire range of variations in α and β. However, the ability to include the temperature gradient in the final derivation was direct consequence of the change of the delay shift formulation. In other words, even though we are not fully capturing the dynamic of the thermal expansion, spatial continuity of the temperature change field is preserved by including the temperature gradient in the formulation in form of the integrator part in (2.16). This effect will be seen in the experimental results shown in the next chapter.

Chapter 3

Ultrasound Temperature Estimation Models: Experimental Results and Discussions

In order to compare different temperature estimation models, several *in vitro* experiments were conducted. In each experiment RF data was collected at high frame rate (in the order of 100 frames per second) using the system described in [41]. The displacement field was then calculated based on the algorithm introduced in [38] and is briefly described below.

3.1 Displacement Estimation Based on Speckle Tracking

Temperature changes create displacements in the order of few microns in the backscattered echos. The system used for collecting all data was working at 40 MHz clock rate which created about 18.7 μm spatial resolution at 1500 m/s speed of sound. Hence, a sub-sample speckle tracking algorithm was required. Simon *et al.* [38] described a method based on zero crossing point of the complex cross correlation phase which is capable of detecting sub-sample displacement without further interpolation. We used the same method throughout our experiments to estimate the frame-to-frame displacement field. In this method, first the analytic (in-phase and quadrature) signal is acquired

from the RF data in two successive frames using Hilbert transform. A short duration of this data is then selected using a rectangular window of size M. The data from most recent frame is then passed through a delay network with lags -1, 0 and 1 and its complex cross correlation with the data form previous frame is calculated. The phase of these cross correlation values are then used to find the zero crossing point using a linear approximation. A block diagram of this procedure is depicted in Fig. (3.1).

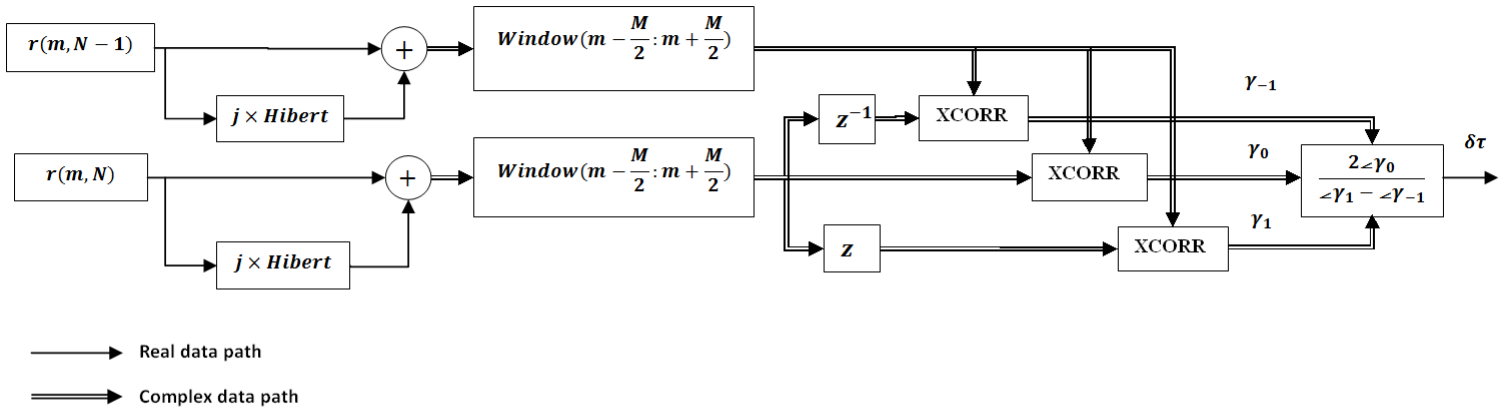

Figure 3.1: Block diagram of sub-sample displacement estimation procedure.

3.2 Wire Heating in Tissue Mimicking Phantom

To create a controlled temperature change we performed an *in vitro* experiment without using HIFU as the heating soruce. A thin resistive Nichrome wire (32 AWG) was embedded in a tissue mimicking phantom which was prepared based on the method described in [51]. The wire was 15 cm long and 0.25 mm thick with 4.5 ohms resistance. A 3V DC source was applied to both ends of the wire which created around 667 milliamps of current for 13 seconds. RF data was acquired before, during and after the heating in a plane cross sectional to the wire in M2D mode[1] . RF data was collected using a L14-5/38 linear array (LA) probe and the SonixRP machine with research interface (Ultrasonix, BC, CA). A needle thermocouple (HYP-1 Omega, Philadelphia, PA) was inserted into the phantom very close to the heating wire. During experiment, temperature data from the thermocouple was collected at 100 frames per second. A schematic of the experiment setup is shown in Fig. (3.1). Using this method, a symmetric cylindrical temperature change can be created around the wire which can help us in understanding differences in different temperature estimation models.

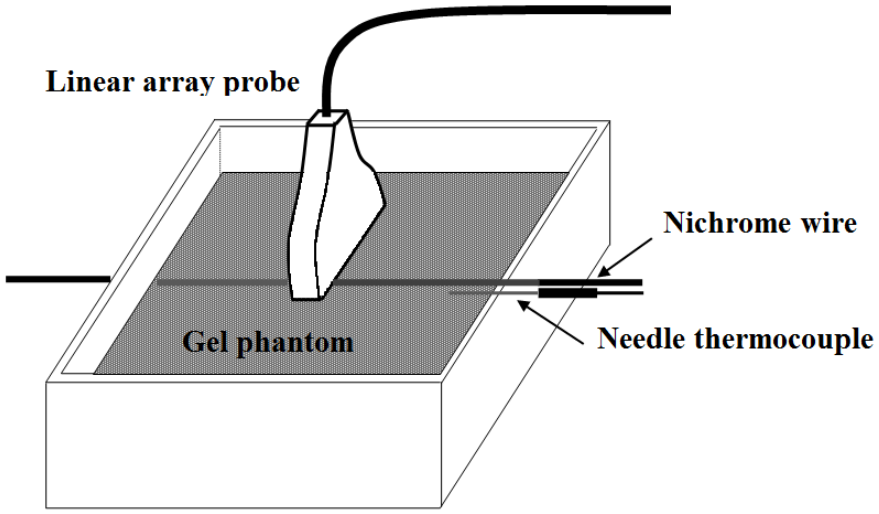

Figure 3.1: Experiment setup used for imaging of the resistive wire in gel phantom.

[1] M2D-mode simply refers to acquiring RF data frames with limited extent in a straightforward extension of the familiar M-mode imaging.

3.3 Subtherapeutic Shots in Blocks of Bovine Heart Tissues

An experiment was performed to estimated the temperature during subtherapeutic HIFU shots in the bovine heart tissues. Blocks of bovine heart tissue with $5 \times 5 \times 5$ cm^3 dimensions were positioned in a custom made holder with two open sides for receiving imaging and HIFU beams. A full concave array was used for applying subtherapeutic HIFU shots for a total duration of 2 seconds. A needle thermocouple was used to simultaneously record the temperature at a point close to the focus of the HIFU transducer. A linear array probe positioned in a cross-sectional configuration was used for imaging before, during and after the HIFU shots. A schematic of the experiment setup is shown in Fig. (3.2).

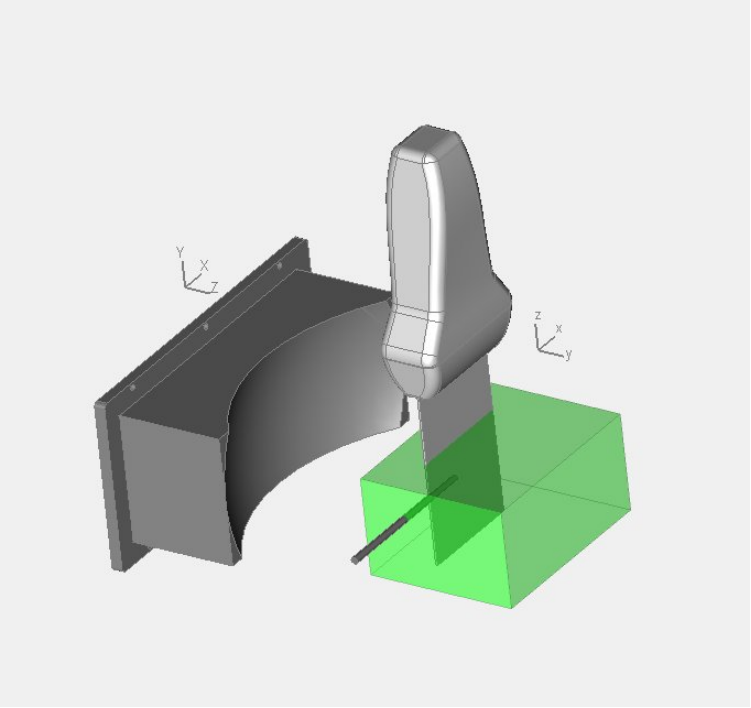

Figure 3.2: Experiment setup used for imaging of the subtherapeutic HIFU shots in the blocks of bovine heart tissues (courtesy of former UISPL member Dr. John R. Ballard).

3.4 Data Processing

In all experiments the M2D data was collected before, during and after the heating procedure with an imaging pulse at 7.5 MHz. A cross correlation kernel length of about 9λ (1.84 mm) was used for all experiments to calculate the displacement field. The incremental displacement field was passed through the axial filter described in (2.15). For heart tissue experiments α and β were set to $3 \times 10^{-4}\ ^{\circ}\mathrm{C}^{-1}$ and $2 \times 10^{-3}\ ^{\circ}\mathrm{C}^{-1}$, respectively based on the average values of thermal coefficients for soft tissue [52],[53]. For gel phantom experiment α and β were set to $2 \times 10^{-4}\ ^{\circ}\mathrm{C}^{-1}$ and $2 \times 10^{-3}\ ^{\circ}\mathrm{C}^{-1}$, respectively based on the average values from the slow heating experiments of the tissue mimicking phantoms reported in [38] and [54].

The integrator part of the axial filter in (2.15) was also applied in the reverse direction to compensate for the group delay.

After performing the axial processing, the data is passed through a frame-to-frame accumulator followed by a low-pass filer with the cut off frequency of 1.5 Hz to create the final estimated temperature. In each experiment, the baseline temperature was measured and used to map the estimated temperature rise to the absolute temperature.

In order to compare the RESF temperature reconstruction model with the δ-ESF model, the displacement data was also processed using a wide-band axial differentiator and a FIR band limited differentiator with a length of 64 as described in [38]. In both experiments, we exclude the use of any 2D filtering post temperature calculations. For example, the (2D+Time) BHTE-inspired filter proposed in [48] was not used here. This approach was effective in removing temperature artifacts inconsistent with the physical model of temperature evolution in tissue media. However, here the objective is to show that the new formulation removes some of these artifacts by virtue of the filtering step implied by equation (2.15).

3.5 Results

3.5.1 Heating Wire Phantom Results

In order to demonstrate the ability of the RESF method in correcting some of the temperature artifacts seen in the δ-ESF model, we first present the results for heating the

thin resistive wire embedded in the tissue mimicking phantom. Fig. (3.3) and (3.4) show the axial-lateral distribution of the estimated temperature using the δ-ESF model and the RESF model respectively. While the δ-ESF model shows rapid temperature fluctuations and ripples, mostly due to thermal lens effect, the RESF model has created a more localized 2-D temperature map consistent with the expected temperature distribution around the heated wire.

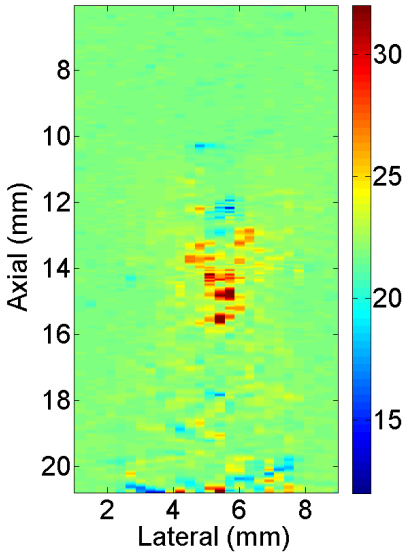

Figure 3.3: Axial-lateral distribution of the estimated temperature around the heated wire using δ-ESF model at peak temperature.

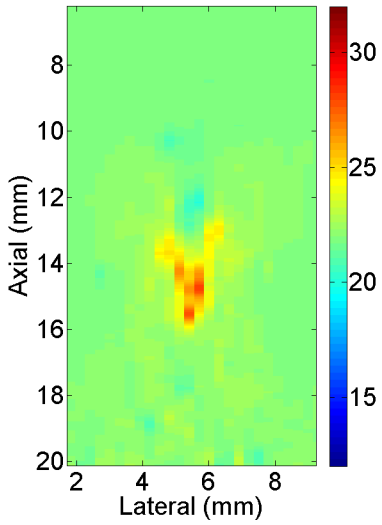

Figure 3.4: Axial-lateral distribution of the estimated temperature around the heated wire using RESF model at peak temperature.

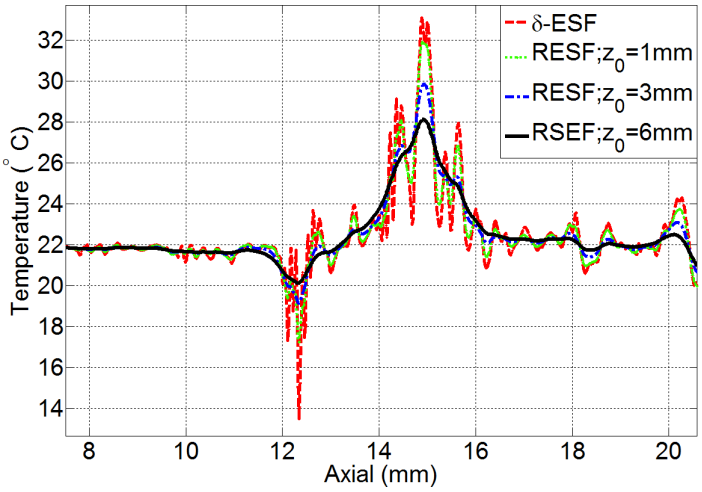

Figure 3.5: Axial distribution of the estimated temperature around the heated wire based on RESF model for $z_0 = 1$ mm, $z_0 = 3$ mm and $z_0 = 6$ mm along with δ-ESF result.

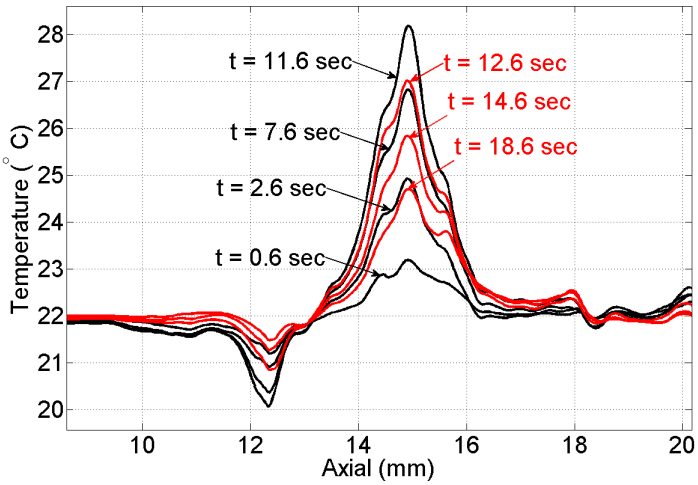

Figure 3.6: Estimated temperature based on the RESF model with z_0= 6 mm at different heating (solid black) and cooling (solid red) time instances.

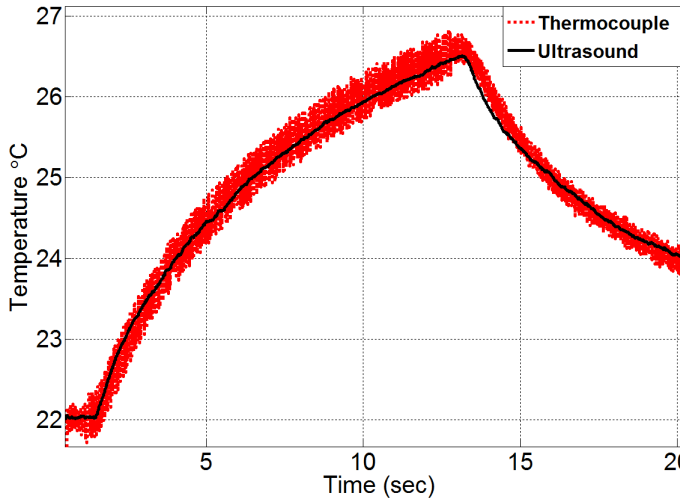

Figure 3.7: Ultrasound estimated temperature (solid black) and thermocouple reading (dotted red) very close to the heated wire.

Fig. (3.5) shows the axial distribution of the estimated temperature using the δ-ESF model and the RESF model with different values of z_0. As it can be seen the RESF suppresses most of the rapid fluctuations close to the heating center, partly caused

by the thermal lens effect. Fig. (3.6) shows the axial distribution of the estimated temperature using the RESF model with $z_0 = 6$ mm at different time instances during heating and cooling cycles. It can be seen that the RESF model has resulted in a localized temperature map with a subtle elevation in the temperature distribution tail during cooling cycle which can be attributed to the diffusion process.

Fig. (3.7) shows the thermocouple data along with the estimated temperature of a point at similar distance from the wire. As it can be seen there is a good agreement between the two data sets in terms of the extent of temperature change without using additional scaling. The estimated temperature rise and fall also show strong consistency with the thermocouple data.

3.5.2 HIFU Acoustic Field and Energy Dose

Creating subtherapeutic temperature changes using HIFU requires careful measurement of the delivered acoustic power. Accurate measurement of the delivered energy requires *in situ* measurements which is not possible in most cases either due to measuring tool limitations or invasive nature of the procedure. However, in water and electrical power measurements can provide an estimate of the delivered acoustic energy which can be then used to estimate the corresponding temperature elevation. The subtherapeutic HIFU beam used in our experiments was produced by the DMUA transducer when geometrically focused. Fig. (3.8)(a) shows a simulated normalized intensity profile of the HIFU beam used. The focal spot forming at the center extends by about 2 mm axially and about 0.4 mm laterally. This simulation was computed by an angular spectrum approach with the elevation-lateral input plane pre-calculated using a Rayleigh Sommerfeld simulation [55]. Using a finite difference time domain (FDTD) method, the corresponding temperature profile based on the normalized acoustic field was presented in [1] which is shown in Fig. (3.8)(b). As it can be seen the the temperature profile is confined within the focus region of the HIFU beam.

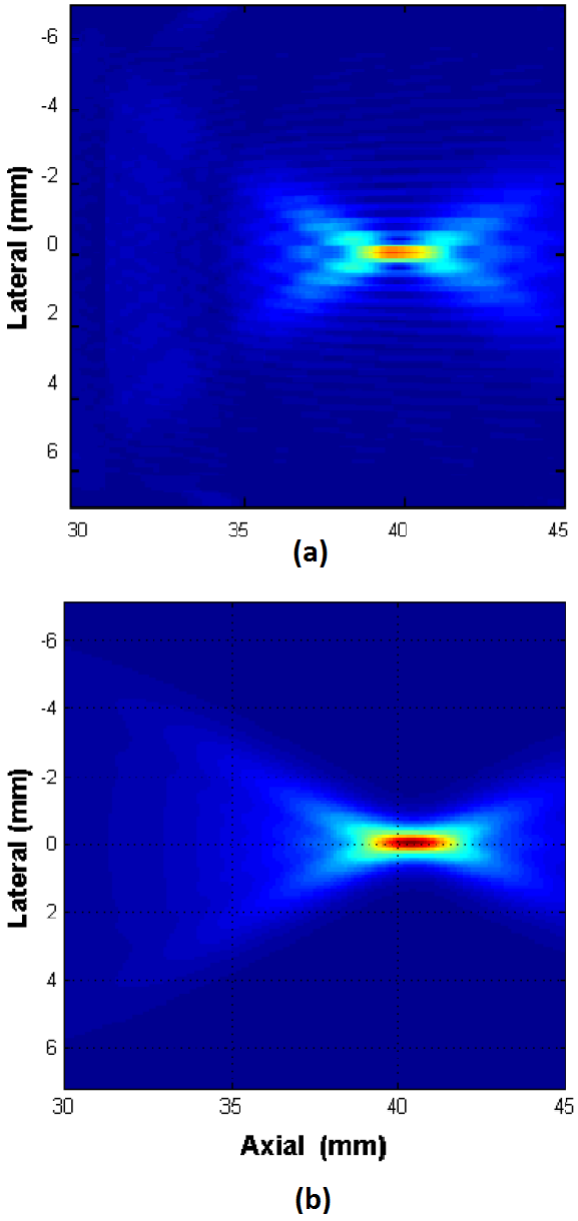

Figure 3.8: Simulated axial-lateral pattern of the HIFU beam (a) and the corresponding temperature pattern (b).

In [1] the same array was used to test the corresponding power using a cone acoustic power meter at different excitation voltages and for different waveforms. The setup

and the test results are shown in Fig. (3.9) (a) and (b) respectively. Experimental results showed that in order to maintain within the subtherapeutic temperature ranges (10-15 °C temperature rise), an acoustic power of 5 Watts or less is required. Hence, throughout our experiments the excitation voltage was kept below 300 mV.

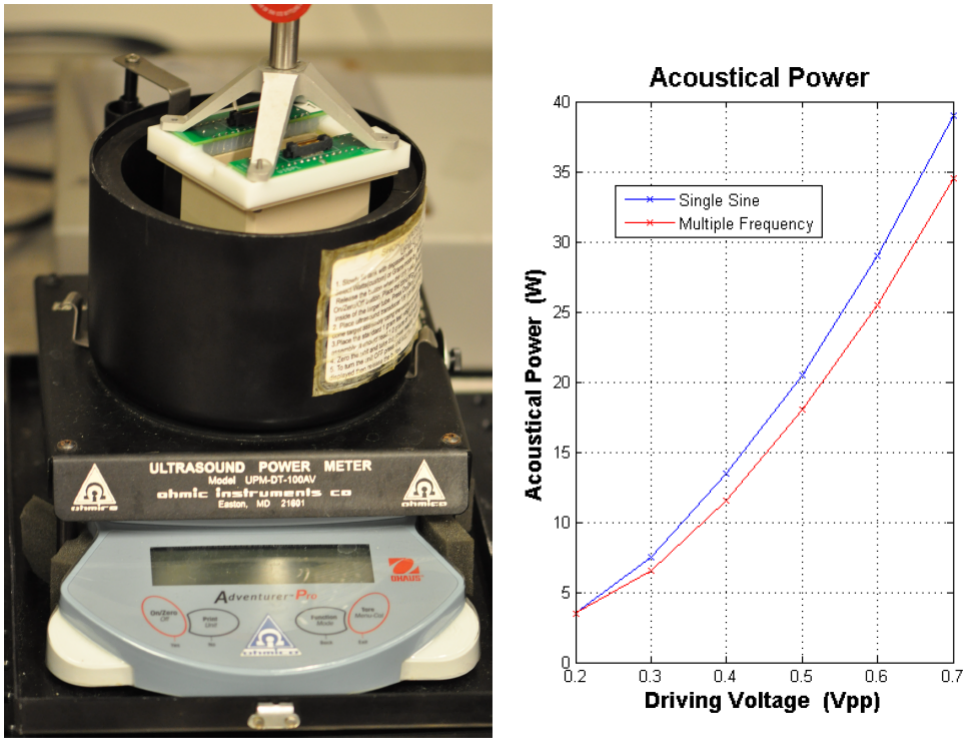

(a) (b)

Figure 3.9: DMUA and acoustic power meter setup (a), and results of acoustic power tests (b) [1].

3.5.3 Results of Subtherapeutic Shots in Bovine Heart Tissue

In order to evaluate the performance of the RESF model in soft tissues, we present the results of tracking temperature during administrating subtherapeutic HIFU shots in blocks of bovine heart tissues. The baseline temperature was measured around 24 °C using a needle thermocouple inserted into tissue block in a plane in parallel to the imaging plane and behind the heating focus. Fig. (3.10) shows the axial-lateral

distribution of the estimated temperature using different methods. Fig. (3.10) (a) shows the result of δ-ESF without further processing. Similar to wire phantom results, same artifacts degrade the spatial distribution of the estimated temperature where rapid temperature fluctuations are seen near the focus as well as behind the focus. These can be mostly attributed to the thermal lens aberration effect. In addition to the thermal lens, speckle tracking artifacts can be magnified due to the inherent amplification of the high frequency components implied by the wide-band differentiator in the δ-ESF model. Fig. (3.10) (b) shows the result of δ-ESF model followed by a length 64 Hamming FIR filter in the axial direction. The smoothing created by the low pass filter has recovered most of the spatial consistencies of the temperature field. Fig. (3.10) (c) shows the result of the RESF model where the same smoothing effect as with the FIR filter has created a more spatially confined temperature profile. During this experiment, self heating of the thermocouple also created a temperature pattern in all three cases with needle trace more visible in Fig. (3.10) (b) and (c).

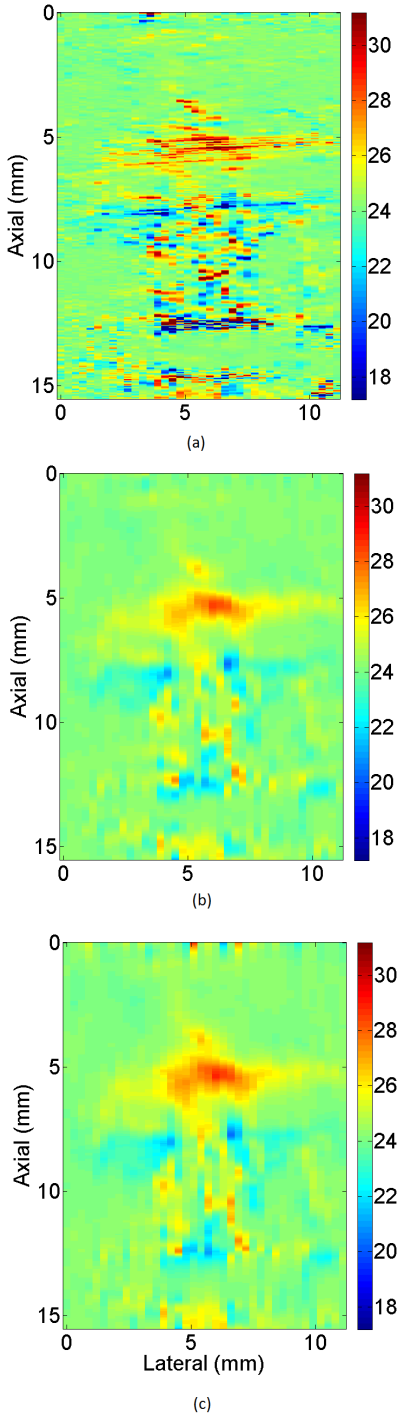

Figure 3.10: Axial-lateral distribution of the estimated temperature near the HIFU focus in the bovine heart tissue using (a) δ-ESF model, (b) δ-ESF model followed by a length 64 Hamming FIR filter and (c) RESF model at peak temperature.

Fig. (3.11) shows the axial-temporal profile of the estimated temperature field using three different methods at a lateral point close to the heating peak. As it can be seen in Fig. (3.11)(a) the temperature profile estimated by the δ-ESF model shows multiple traces of temperature rise with many gaps in between. The HIFU started at 1 sec and continued for two seconds. While some traces follow the start time and end time of the HIFU, some traces show temporal inconsistencies which can make the tracking of true temperature hard. Fig. (3.11)(b) and (c), on the other hand, show more consistent temperature profiles which corroborate with the timing of the HIFU operation and extent of the beam in the axial direction (a 6-dB beamwidth of about 2 mm).

Axial distribution of the temperature profile is shown in Fig. (3.12) at peak temperature time instance. The δ-ESF model shows rapid fluctuations at the focus and slower changes behind the focus. The RESF model and band-limited δ-ESF (using a 64 Hamming FIR filter) show a more consistent axial distribution with a temperature build up at the focus and less artifacts behind the focus.

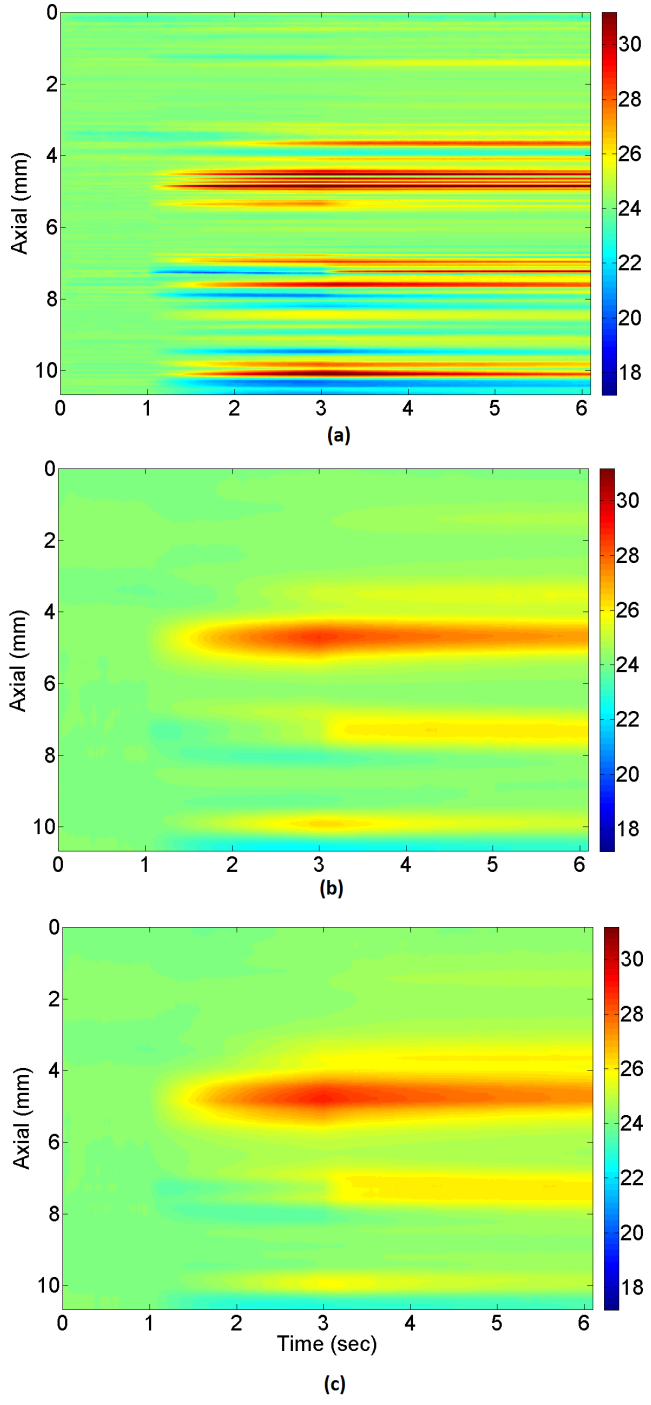

Figure 3.11: Axial-temporal distribution of the estimated temperature along an A-line near the HIFU focus in the bovine heart tissue using (a) δ-ESF model, (b) δ-ESF model followed by a length 64 Hamming FIR filter and (c) RESF model at peak temperature.

In order to evaluate the quantitative accuracy of different methods we compare the result of different temperature estimation methods at a point close to the thermocouple junction. Fig. (3.13) shows the temperature change curve using the δ-ESF (green), band limited δ-ESF (blue), RESF (black) and thermocouple reading (red). While band limited δ-ESF and RESF models show strong agreement with the thermocouple data, the δ-ESF model has resulted in a poor estimate. This can be a largely attributed to the spatial inconsistencies of the δ-ESF model also seen in the spatial distribution profiles.

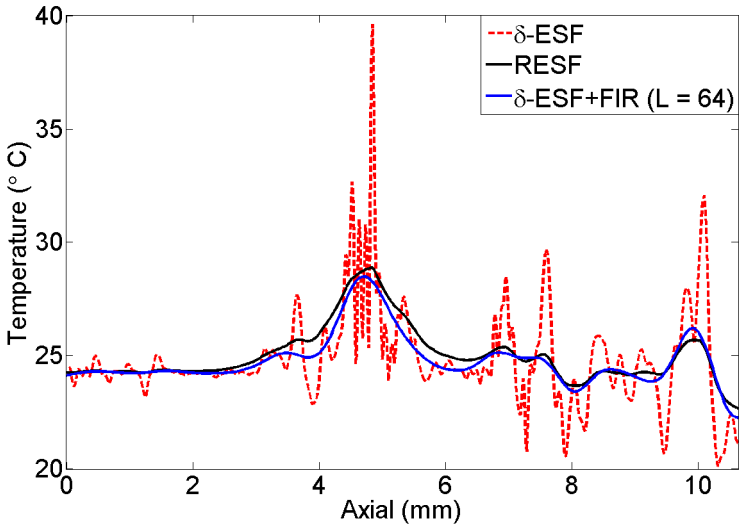

Figure 3.12: Axial distribution of the estimated temperature using δ-ESF model (red), band limited δ-ESF (blue) and RESF model (black) at an A-line close to the peak temperature.

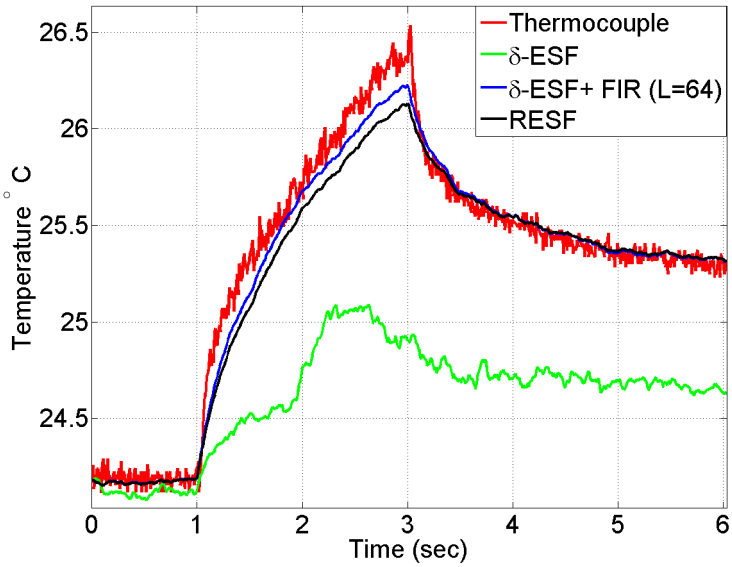

Figure 3.13: Temporal profile of the estimated temperature around the heated wire using δ-ESF (green), band limited δ-ESF (blue), RESF (black) and thermocouple reading (red).

3.6 Discussion and Conclusion

We presented the results of using echo shift based ultrasound temperature estimation based on two models: the δ-ESF and RESF models. In both models, the displacement data was acquired during subtherapeutic temperature changes using one dimensional speckle tracking algorithm based on the zero crossing point of the complex cross correlation phase. From the in vitro and ex vivo experiment results shown in this chapter it can be concluded that the RESF model creates more consistent temperature profiles when compared to the δ-ESF model with no requirement for additional smoothing. The band limited δ-ESF model, however is able to remove most of the artifacts seen in the δ-ESF model by using additional FIR filtering step. The requirement for this post processing step was also highlighted in [38] where authors used spatial bandwidth of the temperature profile to design the band limiting low pass filter. However, this comes at

the additional cost of integrating a long FIR filter which can be a drawback for the real-time implementation. The derivation of the RESF model, on the other hand, resulted in an inherent smoothing feature. In other words, the commutative change of length implied in the model derivation of the RESF model imposed a regularization based on the continuity of the thermal expansion. The parameters of the final model which appeared as a differentiator-integrator operator were based on the tissue properties. It is clear that any post processing used for smoothing the δ-ESF model can be also added in the RESF model for further filtering but it will introduce additional implementation cost. The RESF model is consistent with the δ-ESF model such that by changing an effective recursion length z_0 (introduced in the previous chapter) it can convert to the δ-ESF model. This feature makes the RESF model more appealing as it can be treated as a combined reconstruction-smoothing filter with a convenient single pole implementation where parameters are derived from local tissue properties and excludes the need for further ad hoc filtering.

Chapter 4

Ray Tracing Modeling of the Thermal Lens Aberration

Beamforming is an essential process in modern ultrasound imaging. Most beamforming methods assume a constant speed of sound for image formation, which is justified on the basis of small variations in speed of sound in soft tissues. When this assumption is not valid, however, ultrasound beam distortion due to aberration can occur. In conventional imaging, the effects of aberrations may be mild spatial mis-registration to more severe loss of contrast depending on the severity and the location of the aberration. In the context of temperature imaging, the imaging beam suffers aberrations as it traverses the heated tissue, especially near temperature gradients [38]. This thermoacoustic lens effect results from the temperature dependency on the speed of sound, which has been studied in the literature [2]. In most cases, speed of sound increases with temperature rise in water bearing tissues and decreases in fatty tissues [2].

Figure 4.1 shows the speed of sound as a function of temperature in blood and liver tissue. As it can be seen both media show a quadratic dependency of speed of sound to temperature with a maximum that occurs in 45-55 °C range. Due to this dependency, highly localized temperature changes (e.g. HIFU hyperthermia) create a medium with highly variant speed of sound near the focus. These variations are not taken into account when conventional beamforming is used to compute the echo RF data from points distal to the heated region. This results in minute changes in echo locations, which appear

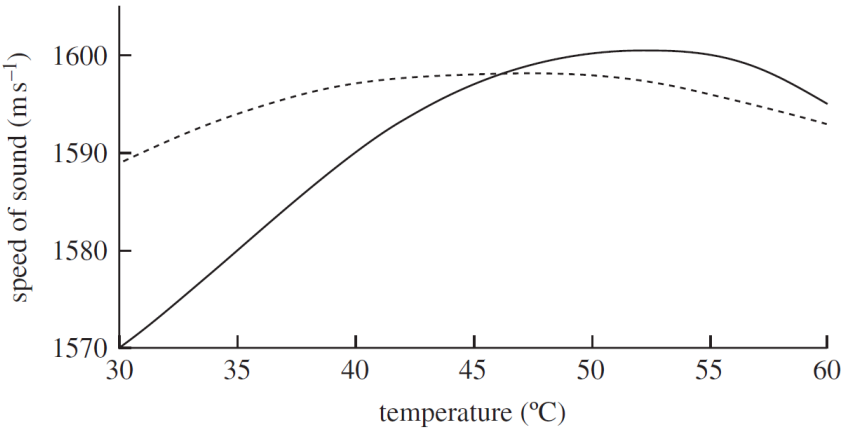

Figure 4.1: Speed of sound variations with temperature in: liver (dashed line) and blood (solid line)[2].

as artifacts in temperature change. These thermal lensing artifacts have characteristic spatial frequency pattern that can be filtered out by 2D spatial filtering [38] or spatial compounding [45].

Any attempt to cancel thermal lensing artifacts would require a full knowledge of speed of sound distribution throughout the interrogated tissue which is generally not feasible. In this chapter we present a variational method for ray tracing modeling of the beam aberration near the focus. Although the results are not directly applicable to the artifact cancellation in the temperature estimation, they provide a quantitative measure of the beam aberration. This can be useful in the assessment of the spatial extent of the artifact seen in the temperature estimation and the spatial distribution of the energy delivery via HIFU.

4.1 Variational Formulation of the Ray Tracing Model

Ultrasound wave propagation through a variable speed of sound region can be explained using models from ray acoustics [56, 57]. Fermat's principle states that a ray of light chooses a travel path between points A and B such that it leaves the optical length stationary under variations in the family of nearby paths. Mathematically this can be

expressed as

$$\delta S = \delta \int_A^B n ds = 0 \tag{4.1}$$

where S is the optical (acoustic) path length, n is the refractive index and ds is the infinitesimal arc length element along the ray path. Equation (4.1) has the form of the calculus of variations in which the Euler-Lagrange's partial differential equation sets the optimality condition. The refractive index $n = c_0/c$ where c_0 is the baseline speed of sound and c is the medium dependent speed of sound. A simple interpretation of the Fermat's principle is the fact that rays of sound travel the path that results in the least time. This is also known as the Fermat's least time principle. Using this principle, Alaniz *et al* [58] presented a method based on two dimensional variational analysis to calculate the beam trajectory when passing through a heated region. Let's assume $c(r)$ to be the speed of sound distribution in a polar coordinate. Based on Fermat's least time, a ray of sound travels along the trajectory $\phi(r)$ which minimizes the following cost function

$$J = \int_{r_s}^{r_e} \frac{1}{c(r)} \sqrt{1 + r^2 (\frac{d\phi(r)}{dr})^2} dr = \int_{r_s}^{r_e} \Gamma(\phi, r) dr \tag{4.2}$$

where r_s and r_e are the radii of the start point and end point of a ray, respectively, with ϕ denoting the angle (in the polar coordinates). Equation (4.2) has the form of a variational cost function in which the solution function should satisfy the following Euler-Lagrange's partial differential equation

$$\frac{d}{dr} \frac{\partial \Gamma(\phi, r)}{\partial (d\phi(r)/dr)} - \frac{\partial \Gamma(\phi, r)}{\partial \phi} = 0 \tag{4.3}$$

Using (4.2) in (4.3) we have the following optimality condition

$$\frac{d\phi}{dr} = \frac{K c(r)}{r \sqrt{r^2 - K^2 c^2(r)}} \tag{4.4}$$

where K is an integration constant which can be defined by initial condition of the ray starting point according to

$$K = \frac{(\frac{d\phi}{dr})|_{r_0} r_0^2}{c(r_0) \sqrt{1 + (\frac{d\phi}{dr})|_{r_0} r_0^2}} \tag{4.5}$$

where r_0 is the radius of the initial point that the ray is fired. A closed form solution of (4.4) exists only for the case that speed of sound is linearly dependent on the radial distance r [59], but the equation is amenable to numerical solutions.

4.2 Numerical Implementation and Results

In order to simulate the thermal lens aberration we define a grid of points in the polar coordinate with sources located on the top row of the grid. The assumption is that each source produces a plane wave traveling in a straight direction under the uniform speed of sound distribution condition. Hence, a ray is assigned to each source to represent its wave front's trajectory. For each trajectory there is a breaking point in which the radial distance is equal to Kc in (4.4). From this point on, the trajectory is the mirrored version of the points already computed with respect to the line connecting the origin and the breaking point. Hence all calculations are performed for half of the path and the other half is derived based on a reflection transformation.

4.2.1 Speed of sound variation model

For simplicity, the speed of sound is modeled as a function of the radial distance from the origin. This model can represent the situation where the center of focused heating is located at the origin with symmetrical radial distribution in a homogeneous medium. The two dimensional heat kernel has the following form [60]

$$G(t, r) = \frac{1}{4\pi t} e^{-\frac{r^2}{4t}} \tag{4.6}$$

In a small vicinity of the temperature unit this kernel can be approximated as

$$G(t, r) \approx \frac{1}{4\pi t} \frac{1}{1 + \frac{r^2}{4t}} \tag{4.7}$$

Based on equation (4.7) the speed of sound dependency is modeled as

$$c(r) = c_0 + \frac{\Delta c}{1 + k^2 (r - r_0)^2} \tag{4.8}$$

where it allows for a radial dependency. The scaling factor k controls the spatial extent of changes in the speed of sound (a larger k results in a more spatially confined change in

speed of sound) and r_0 allows for a radial shift in the change of speed of sound peak. The quadratic dependency of the speed of sound in temperature, which is the case for many soft tissues, suggests that after certain temperature rise the speed of speed reduces with temperature. Considering a focused heating this can lead to a speed of sound pattern that resembles a ring in a two dimensional cross section. The model described in (4.8) is capable of representing this type of variations in speed of sound. Fig. (4.2) shows the speed of sound profiles for different scaling factor k where the baseline speed of sound is 1500 m/s and a maximum change of 20 m/s occurs. The value of k can be adjusted to reflect the spatial extent of the focused heating. Fig. (4.3) depicts the radial variation of the speed of sound along the x axis for $k = 5000$ and different shift values in the center of speed of sound change peak. This feature allows for modeling of changes in the speed of sound when heat diffusion occurs. An example of this situation is when there is a high temperature change at the focus and lower temperature changes due to diffusion at the neighboring points. This temperature distribution can create a null in the speed of sound profile such that the maximum of the speed of sound moves away from the center.

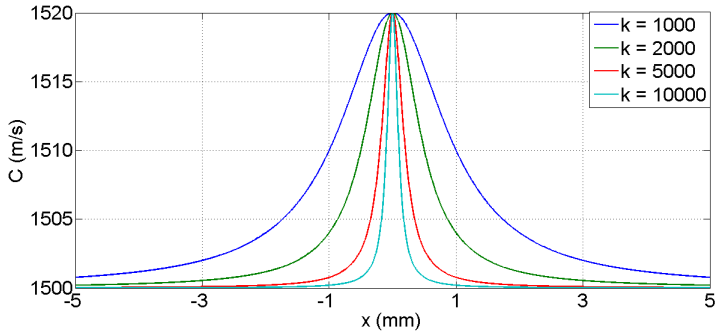

Figure 4.2: Speed of sound variations as a function of radial distance along the x axis for different values of k.

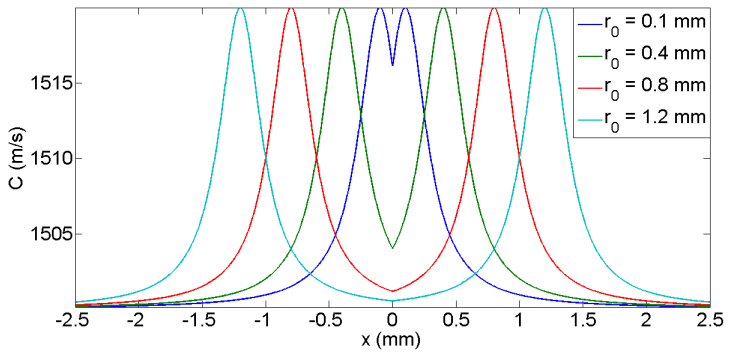

Figure 4.3: Speed of sound variations as a function of radial distance along the x axis for $k = 5000$ and different values of r_0.

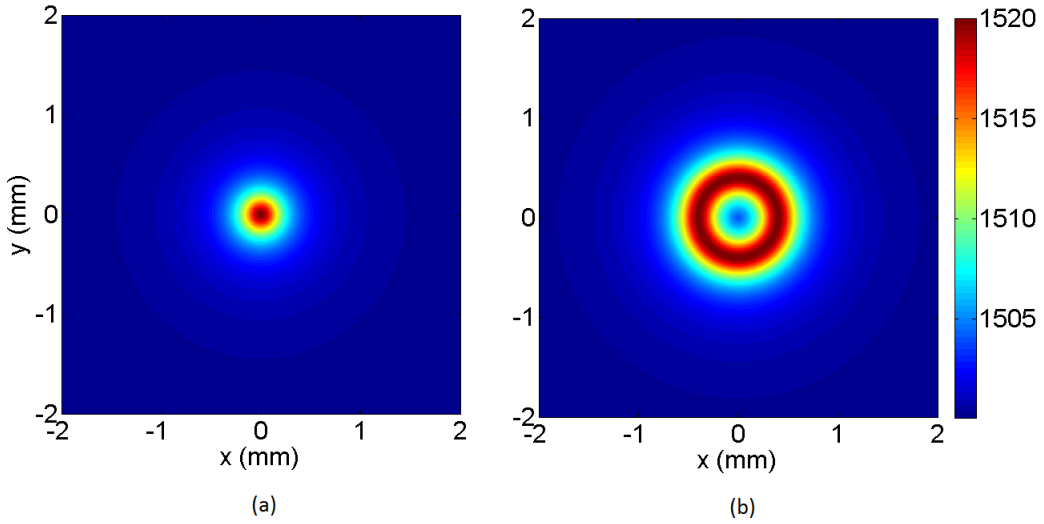

Figure 4.4: Spatial profile of speed of sound variations as a function of radial distance for $k = 5000$ and: (a) $r_0 = 0$ and (b) $r_0 = 0.4$ mm.

4.2.2 Numerical Solution with Variable Step Size

In order to numerically solve (4.4) a starting dr of 10^{-12} m is selected. However, as the trajectory gets closer to the breaking point a finer step size is required as the error accumulation can be severe. Hence we use a variable step size which scales down

dr based on the values of the radical in (4.4) and up to a minimum dr of 10^{-14} m. Without such a variable step size points near the breaking point show poor accuracy and using the reflection transformation creates a large error in the overall trajectory calculation. A C/MEX routine was created with the capability of accepting number of transmitting sources, locations of the sources, speed of sound profile as a function of radial distance and maximum number of points in a single trajectory. An example of the program performance is shown in Fig.(4.5) where the ray trajectories are projected on a spatial representation of a nonuniform speed of sound. In this particular example we assumed a ring speed of sound profile. An example of this situation is when the center of focused heating is located at the origin and temperature rise exceeds the peak point of a quadratic speed of sound-temperature profile. The baseline speed of sound was assumed to be 1500 m/s with and the maximum change was 50 m/s. As it can be seen Fig.(4.5) rays traveling through the heated region bend toward the higher speed of sound region as it is intuitively expected from Fermat's least time principle while the direction of those passing through the uniform speed of sound region remain unchanged.

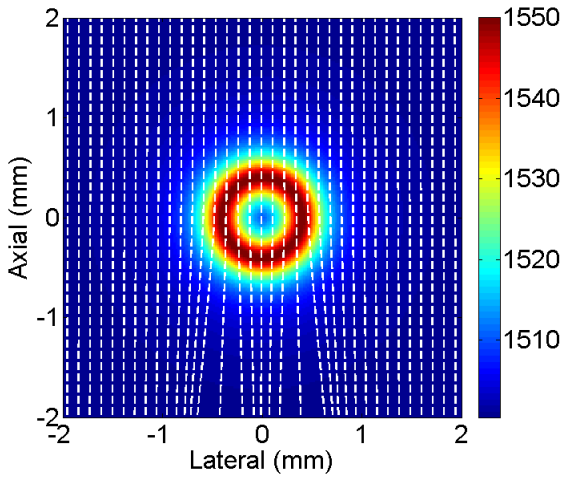

Figure 4.5: Ray trajectories overlaid on a spatial representation of speed of sound variations.

4.3 Simulation Results

Based on the presented model and a given speed of sound profile it is possible to quantify the amount of aberration caused by the nonuniform speed of sound. Given that the trajectory of rays for a uniform speed of sound is a straight line, any horizontal deviation can be regarded as a measure of the aberration. Here we present the results of the simulation model for different speed of sound patterns which can occur during HIFU operation and imaging.

4.3.1 Low Temperature Rise with Linear Increasing Speed of Sound

In most water bearing tissues the speed of sound increases with a low temperature rise. Starting from a baseline temperature, this dependency can be modeled as a linear function with a positive slope. We assume a baseline speed of sound of 1500 m/s and a 20 m/s change based on the equation (4.8) with k = 5000 and r_0= 0. Fig. (4.6)(a) shows the deviation from the straight line as a displacement field in micrometer with the corresponding speed of sound profile shown in (b). As it can be seen lateral deviation starts at the origin which corresponds to maximum speed of sound. The rays on the right side of the origin experience a positive deviation while the rays on the left side undergo a negative deviation. The extent of this deviation is more than 40 μm at points close to the center and it tapers off with distance from the center. This deviation creates a skirt like pattern where at 10 μm displacement it extends about 1 mm at 2 mm below the origin. It is also noticed that the rays passing right through the origin experience no deviation as expected.

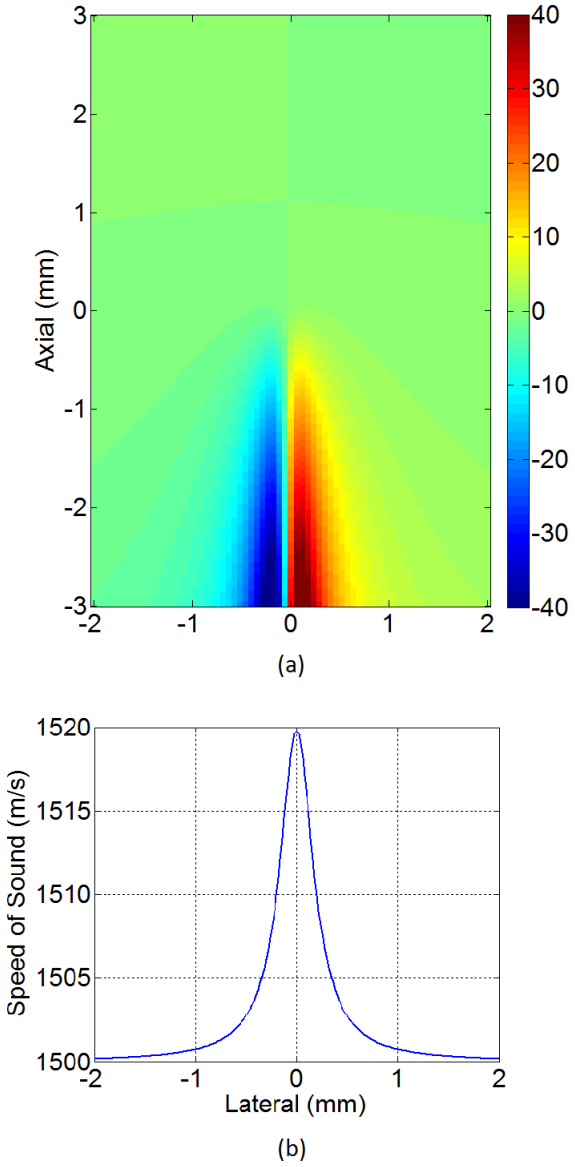

Figure 4.6: Lateral ray deviation due to aberration: (a) displacement field (colorbar in μm), (b) corresponding speed of sound profile (small positive speed of sound change).

4.3.2 Low Temperature Rise with Linear Decreasing Speed of Sound

In most fatty tissues the speed of sound decreases with temperature for low temperature changes such that this dependency can be modeled as a linear function with a negative slope. Here we model a small negative change in the speed of sound based on the (4.8) with a baseline value of 1500 m/s, k = 5000, r_0=0 and a -20 m/s change. Fig. (4.7) (a) and (b) show the lateral deviation profile and the corresponding speed of sound respectively. From the lateral deviation profile it can be seen that the ray on the left side of the origin bend toward the right half plane while the rays on the right side of the origin bend to toward the left half plane. The extent of the aberration is similar to the previous case where a 10 μm lateral deviation has 1 mm lateral width at 2 mm below the origin.

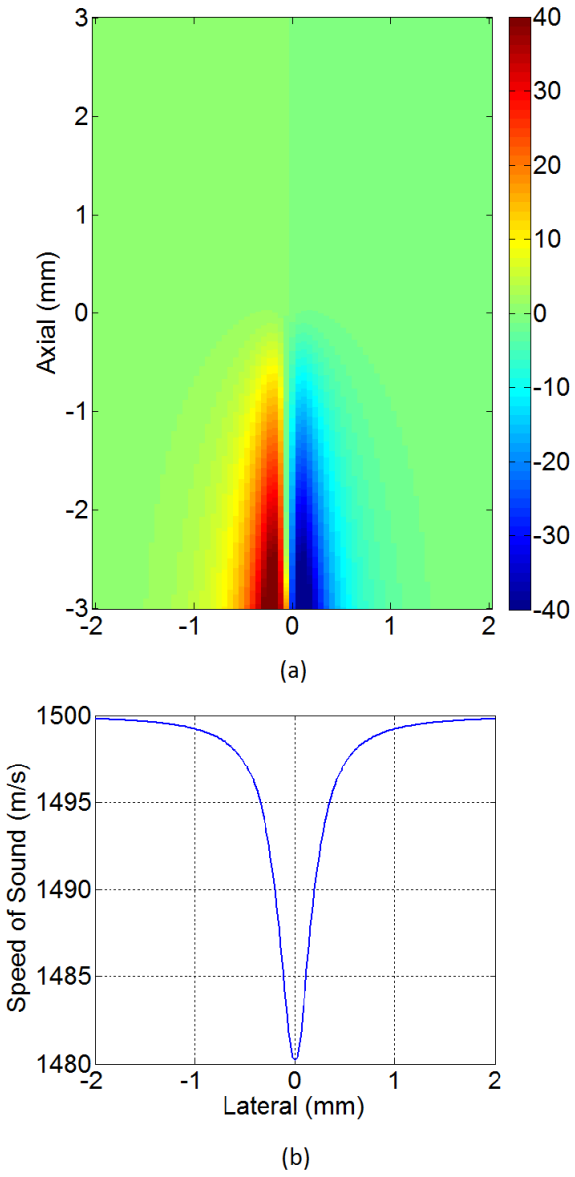

Figure 4.7: Lateral ray deviation due to aberration: (a) displacement field (colorbar in μm), (b) corresponding speed of sound profile (small negative speed of sound change).

4.3.3 High Temperature Rise with Quadratic Speed of Sound

Most soft tissues show a quadratic speed of sound temperature dependency at higher temperatures. This means that speed of sound reduces with temperature above a certain value. To model the effect of this dependency on the ultrasound aberration we considered a ring profile for the speed of sound where the baseline speed of sound was 1500 m/s and a high temperature change caused a maximum change of 50 m/s at 0.4 mm radial distance from the origin. Fig. (4.8) shows the lateral deviation profile in micrometer in (a) and the corresponding speed of sound in (b). From Fig. (4.8) (a) it can be seen the lateral deviation profile is divided into four different regions with different direction of deviations. The speed of sound ring profile has caused the rays at both sides of the origin experience positive and negative deviations in an anti symmetrical manner. The aberration skirt covers a larger lateral extent compared to the previous cases where the 10 μm deviation at 2 mm below the origin extends about 3 mm laterally.

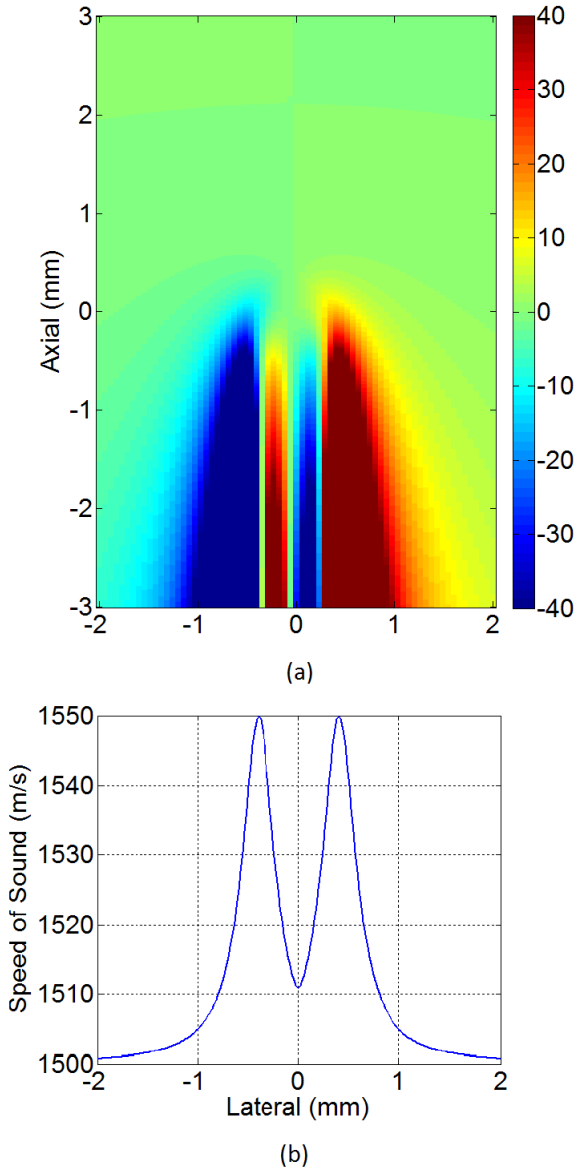

Figure 4.8: Lateral ray deviation due to aberration: (a) displacement field (colorbar in μm), (b) corresponding speed of sound profile (large positive speed of sound change).

4.4 Discussion and Conclusion

We presented a ray tracing modeling of the ultrasound aberration due to variable speed of sound. The model was based on the numerical solution of the Fermat's least time principle. From the examples shown, it is clear that localized changes in the speed of sound causes ultrasound beams to travel in a curved path such that the total optical distance is minimized. We considered three different cases with different speed of sound heterogeneity profiles and extent of the variations. It was observed that in all cases the simulation model suggested that lateral deviation of the ultrasound beams occur at and behind the focus. The extent of this deviation was shown to be in order of tens of microns for each ray but it becomes wider with the distance from the focus. When using diagnostic probes for imaging, the large lateral extent of the point spread function, which is usually in the order of hundreds of microns, further spreads this effect. This qualitative observations are theoretical confirmation and validation of the thermal lens artifact repeatedly seen during echo based ultrasound thermography. In order to further quantify the resulting temperature error when using speckle tracking echo shifts a scattering model is required which is beyond the scope of this thesis.

Chapter 5

Adaptive and Model Based Techniques for *In Vivo* Ultrasound Temperature Estimation

The echo shift based temperature estimation model is based on the assumption that displacement seen in the RF echoes are only due to change in speed of sound and thermal expansion. However, *in vivo* natural motions can create displacements that if not treated properly, can adversely affect the performance of the echo shift based temperature estimation methods. These motions can appear as artifactual strain patterns blended with the temperature induced echo strain. Due to connectivity of the different layers of tissue, any mechanical stress originated in a muscle or organ can propagate in a wider region depending on the amplitude of the stress and composition of the tissue. For example, the strain pattern created by respiration or gasping can propagate in a wider range than the strain caused by a pulsating blood vessel. Hence, in terms of strain pattern, large scale motions like breathing are more global effects while pulsation is more localized. Regardless of the spatial distribution, both of these effects are quasi periodic, but the frequencies differ greatly. This temporal behavior suggests that frequency selective temporal filtering of thermography data could be useful in improving its sensitivity and specificity. However, the shared temporal bandwidth of the deformations and induced therapeutic temperature change requires the selective filters to be

also aware of both spatial and temporal variations in order to preserve the dynamic of the true temperature change. This can be seen in Fig. (5.1) where RESF temperature reconstruction model has been applied on the displacement data during an *in vivo* experiment. The details of the experiment setup and material will be explained in the subsequent sections. Fig. (5.1) (a) shows the temporal profile while Fig. (5.1)(b) depicts the corresponding frequency domain representation. All profiles are normalized to have unity mean value. The Welsh's method was used for estimation of the power spectral density. The four different temporal profiles are selected from spatially different points in the imaging plane. Different profiles can be attributed to different events as the following: (blue) true temperature change, (red) true temperature change blended with gasping artifacts, (green) gasping profile and (black) blood vessel pulsation profile. As it can be seen in Fig. (5.1)(b) the different profiles share almost the same bandwidth which makes it impractical to use frequency selective filters to extract temperature.

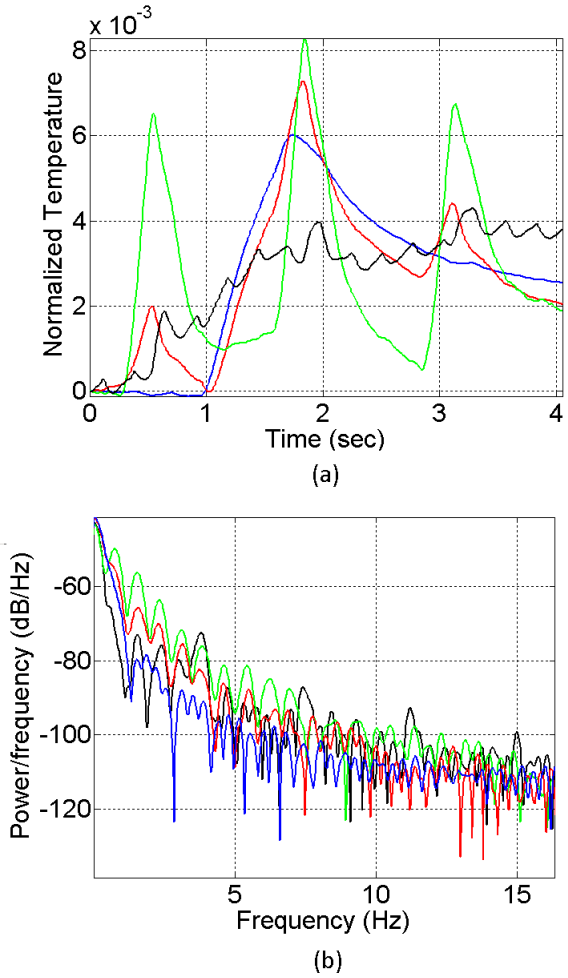

Figure 5.1: Normalized temperature profiles at different points during an *in vivo* experiment: (a) time domain (b) corresponding frequency domain using Wlesh's power spectral estimation method.

5.1 Adaptive Filter Approach

In spite of frequency bandwidth overlap between artifacts sourcing from different events and true temperature during *in vivo* ultrasound temperature estimation, there are aspects of the data that makes adaptive techniques good candidates for separating these

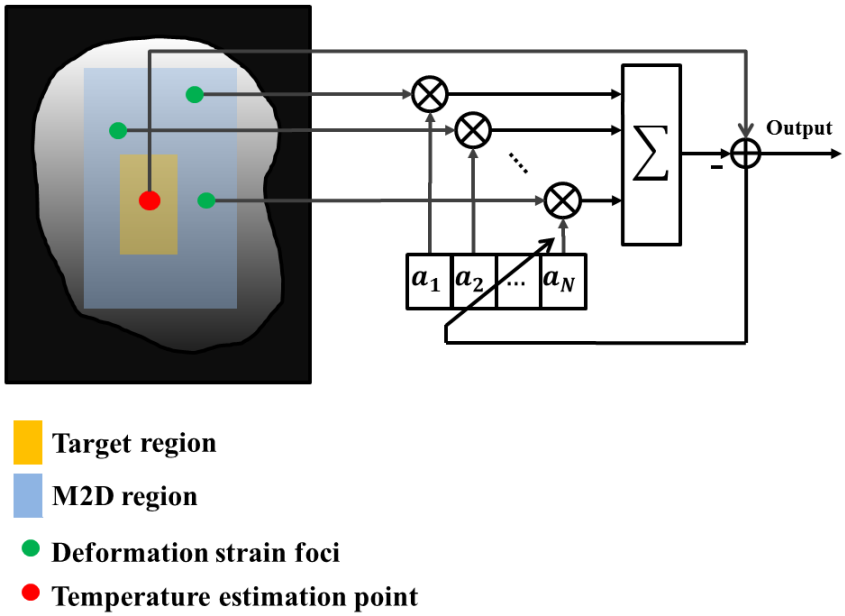

Figure 5.2: Adaptive filter configuration. N observation points are selected outside the heated region based on pre-heating analysis of tissue motions and deformations (Green dots). A temperature reference point is selected from the heated region (Red dot) based on the target of the focus and/or the analysis of the initial heating rate immediately after the HIFU pulse is applied. The error function shown in the schematics controls the adaptation according to an appropriate algorithm, e.g. NLMS [3].

events. For examples, most of the natural motion related artifacts are quasi periodic and their occurrence is independent of the temperature change mechanism. Another aspect of these artifacts is spatial distribution. A pulsating blood vessel creates mechanical waves which are mostly limited to the vicinity of the vessel. A gasping or breathing motion, on the other hand, creates displacement in a larger region. Most of the translational motions, however, are removed by the differentiator part of the temperature reconstruction filters. Mechanical strains, on the other hand, tend to create distinct foci at different locations in the imaging plane.

Here we present an adaptive technique for dealing with motion deformation artifacts which can greatly enhance the estimation of temperature while maintaining the essential spatial-temporal properties of the temperature field. The method takes advantage of the global availability of the deformation field before HIFU starts to train the coefficients

of an adaptive filter. During therapy, the trained filter is used to remove the motion interference field. Although the temperature and motion fields can share the same bandwidth, the *in vivo* results show that the fact that these two fields are statistically uncorrelated can greatly help in separating them without sacrificing the temperature dynamic.

Lets assume the estimated temperature in the axial-lateral grid point (m, n) and time index k to be $\theta(m, n, k)$. The artifactual temperature of a point outside the heated region due to a strong deformation strain is denoted as $\theta_a(m_i, n_i, k)$ and we collect N such points for interference compensation. Before heating starts, for each time index k, the error is defined as

$$e(m, n, k) = \theta(m, n, k) - \sum_{i=1}^{N} a_i(m, n)\theta_a(m_i, n_i, k) \tag{5.1}$$

where $a_i(m, n)$'s are the coefficients of the adaptive filter for grid point (m, n). Using a Normalized Least Mean Squares (NLMS) method this error is used to find the optimal value of the coefficient vector $\mathbf{a}(m, n) = [a_1(m, n), a_2(m, n), ..., a_N(m, n)]$ using the update equation,

$$\mathbf{a}^{(k+1)}(m, n) = \mathbf{a}^{(k)}(m, n) + \mu e(m, n, k)\frac{\mathbf{t}_{foci}(k)}{\mathbf{t}_{foci}^{T}(k)\mathbf{t}_{foci}(k)} \tag{5.2}$$

where

$\mathbf{t}_{foci}(k) = [\theta_a(m_1, n_1, k), \theta_a(m_2, n_2, k), ..., \theta_a(m_N, n_N, k)]^T$ is a $N \times 1$ vector containing the artifactual temperature data of each training point at time k and μ is the step size. The training phase stops as soon as the artifactual temperature values drop below a defined threshold. Once heating starts the corrected temperature field is calculated as follows

$$\theta_c(m, n, k) = \theta(m, n, k) - \sum_{i=1}^{N} a_i^*(m, n)\theta_a(m_i, n_i, k) \tag{5.3}$$

where θ_c is the motion compensated temperature field and a_i^*s are the entries of the coefficient vector calculated at the last iteration of the NLMS algorithm during the training phase. Fig. (5.2) depicts the diagram of this process where green dots represent the deformation foci and the red dot represents a point from the target region for temperature estimation. The training phase can be repeated for multiple HIFU shots given

that there is enough time for tissue to return to baseline temperature. The essential assumption here is that there is a strong correlation between mechanical deformation foci. It is also crucial to select the training points from points outside the converging region of the HIFU beam as the mechanical and thermal effect of HIFU can create artifact or decorrelation during update phase.

5.2 Model Based Techniques

The key in successful implementation of the adaptive techniques presented in the previous section was global availability of the deformation foci outside the target region. In some cases, however, such training points might not be available or their temporal statistics might change over time (e.g. due to out of plane motion, in-plane disorientation, time-varying specular reflection) which can adversely affect the performance of the motion compensation algorithm. We present a model based temperature tracking method based on the discretization of the bioheat equation. A Kalman filter formulation of the problem is presented which is capable of detecting and skipping erroneous frames via innovation process thresholding and predicting the temperature over those frames using the enforced model.

5.2.1 Dynamic Model Derivation

Heat conduction in a tissue region excited by the acoustic power field P can be formulated using Pennes' bioheat equation [61]

$$\rho C \frac{\partial T}{\partial t} = \kappa \nabla^2 T - w C_b (T - T_a) + P \tag{5.4}$$

where ρ $[kg.m^{-3}]$ is the tissue density, C and C_b $[J.kg^{-1}.^{\circ}C^{-1}]$ are the tissue and blood specific heats respectively, w $[mL.mL^{-1}.s^{-1}]$ is the perfusion rate, κ $[W.^{\circ}C^{-1}]$ is the tissue thermal conductivity in , T and T_b $[^{\circ}C]$ are the tissue and artery blood temperatures, respectively, with P $[W.m^{-3}]$ denoting the acoustic power. Ignoring the blood perfusion and rearranging the equation it follows

$$\frac{\partial T}{\partial t} = D \nabla^2 T + \epsilon P \tag{5.5}$$

where D $[m^2.s^{-1}]$ is the thermal diffusivity and ϵ $[m^3.^{\circ}C.J^{-1}]$ is the absorption coefficient. In order to simplify the model we only consider one dimensional case. By taking a

time derivative from both sides and using a first order spatial derivative approximation

$$\frac{\partial^2 T}{\partial t^2} \approx D\frac{\partial}{\partial t}\frac{T(t,z+\Delta z)+T(t,z-\Delta z)-2T(t,z)}{\Delta z^2}+\epsilon\frac{\partial P}{\partial t} \tag{5.6}$$

By defining an M point spatial grid such that $z = m\Delta z$, $(m = 1, 2, ..., M)$,

$$\frac{\partial^2 T}{\partial t^2} \approx \gamma\frac{\partial}{\partial t}(T(t,m+1)+T(t,m-1)-2T(t,m))+\epsilon\frac{\partial P}{\partial t} \tag{5.7}$$

where γ is defined as $D/\Delta z^2$ and Δz is dropped from the spatial arguments for notation simplicity. For each grid point we define the state variables as

$$\begin{aligned} x_{m,1} &= T(t,m), \\ x_{m,2} &= \dot{x}_{m,1} = \tfrac{\partial}{\partial t}T(t,m) \end{aligned}$$

and using (5.7)

$$\begin{aligned} \dot{x}_{m,1} &= x_{m,2} \\ \dot{x}_{m,2} &= \gamma(x_{m+1,2}+x_{m-1,2}-x_{m,2})+\epsilon\tfrac{\partial P}{\partial t} \end{aligned}$$

Using these equations we can write the state-space equations for states taken around a grid point m for $m = 2, 3, ..., M-1$

$$\begin{pmatrix} \dot{x}_{m-1,1} \\ \dot{x}_{m-1,2} \\ \dot{x}_{m,1} \\ \dot{x}_{m,2} \\ \dot{x}_{m+1,1} \\ \dot{x}_{m+1,2} \end{pmatrix} = \begin{pmatrix} 0 & 1 & 0 & 0 & 0 & 0 \\ 0 & -2\gamma & 0 & \gamma & 0 & 0 \\ 0 & 0 & 0 & 1 & 0 & 0 \\ 0 & \gamma & 0 & -2\gamma & 0 & \gamma \\ 0 & 0 & 0 & 1 & 0 & 0 \\ 0 & 0 & 0 & \gamma & 0 & -2\gamma \end{pmatrix} \begin{pmatrix} x_{m-1,1} \\ x_{m-1,2} \\ x_{m,1} \\ x_{m,2} \\ x_{m+1,1} \\ x_{m+1,2} \end{pmatrix} + \begin{pmatrix} 0 & 0 & 0 & 0 & 0 & 0 \\ 0 & \epsilon & 0 & 0 & 0 & 0 \\ 0 & 0 & 0 & 0 & 0 & 0 \\ 0 & 0 & 0 & \epsilon & 0 & 0 \\ 0 & 0 & 0 & 0 & 0 & 0 \\ 0 & 0 & 0 & 0 & 0 & \epsilon \end{pmatrix} \begin{pmatrix} \frac{\partial}{\partial t}P(t,m-1) \\ \frac{\partial}{\partial t}P(t,m) \\ \frac{\partial}{\partial t}P(t,m+1) \end{pmatrix} \tag{5.8}$$

To enforce a Dirichlet boundary condition, states corresponding to the temperature at two extreme points (at the beginning and at the end) are set to the baseline temperature. The state matrix is block diagonal which can greatly facilitate the calculations

using sparse matrix techniques. Using the temperature reconstruction method based on the displacement estimation technique explained in [38] and [55] the axial temperature distribution for each frame can be calculated. This is in the form of temperature rate which can be applied to the Kalman filter setting as the measurement input. Hence, the measurement equation can be written as

$$\begin{pmatrix} z_1 \\ z_2 \\ \vdots \\ z_M \end{pmatrix} = \begin{pmatrix} 0 & 1 & 0 & 0 & 0 & \cdots & 0 \\ 0 & 0 & 0 & 1 & 0 & \cdots & 0 \\ \vdots & \vdots & \vdots & \vdots & \vdots & \ddots & \\ 0 & 0 & \cdots & & & 0 & 1 \end{pmatrix} \begin{pmatrix} x_{1,1} \\ x_{1,2} \\ \vdots \\ x_{M,1} \\ x_{M,2} \end{pmatrix} \tag{5.9}$$

Hence in matrix form equations (5.8) and (5.9) are

$$\begin{aligned} \dot{x} &= A_c x + B_c u \\ z &= Hx \end{aligned} \tag{5.10}$$

where u is a $M \times 1$ vector containing the time derivative of the input acoustic power at M spatial grid points and it represents the control input. A_c, B_c and H are the corresponding matrices based on equations (5.8) and (5.9) and are functions of time in general.

5.2.2 Kalman Filter Formulation

Given that the tissue thermal properties are known, equation (5.8) and hence (5.10) resemble the state-space model of a standard continuous time Kalman filter. Two approximations were made in these derivations: limiting the spatial domain to one dimension and derivative approximation used in (5.6). These deviations from the true models imply that a modeling error has to be introduced. The measurements are also corrupted by the displacement estimation noise process. Hence a better statistical model accounting for these two errors would be of the following form

$$\begin{aligned} \dot{x} &= A_c x + B_c u + w \\ z &= Hx + v \end{aligned} \tag{5.11}$$

where w and v are $M \times 1$ model error noise and measurement noise vectors respectively and we assume they are uncorrelated. A Gaussian distribution is assumed for modeling and measurement noise processes with diagonal covariance matrices Q and R respectively.

5.2.3 Discrete-Time Kalman Filter

The state-space equations in (5.11) can be discretized using a piecewise constant assumption

$$u(t) = u(t_k) \quad t_k \leq t < t_{k+1} \tag{5.12}$$

From (5.11) we can write the state value at time t_{k+1} based on its previous value at time t_k

$$x(t_{k+1}) = F(t_{k+1}, t_k)x(t_k) + \int_{t_k}^{t_{k+1}} F(t_{k+1}, \tau)[B_c(\tau)u(\tau) + w(\tau)]d\tau \tag{5.13}$$

where $F(t_{k+1}, t_k)$ is the state transition matrix with the following properties [62]

$$\frac{dF(t, t_0)}{dt} = A_c(t)F(t, t_0) \tag{5.14}$$

$$F(t_2, t_0) = F(t_2, t_1)F(t_1, t_0) \quad \forall t_1 \tag{5.15}$$

$$F(t, t) = I \tag{5.16}$$

$$\tag{5.17}$$

Under a cummutativity property [62] the state transition matrix F can be related to the continuous system matrix A_c as follows

$$F(t_{k+1}, t_k) = e^{\int_{t_k}^{t_{k+1}} A_c(\tau)d\tau} \tag{5.18}$$

For a time invariant system matrix A_c this becomes

$$F(t_{k+1}, t_k) = e^{A_c T} \tag{5.19}$$

where T is the sampling period. There are different ways to evaluate the right hand side of (5.19). However we use a first order approximation based on the polynomial series expansion

$$A = F(t_{k+1}, t_k) \approx I + A_c T \tag{5.20}$$

where A is the discrete time state transition matrix. Using (5.19) in (5.13) it follows that $B = B_c T$. With a random initialization, the state vector and its covariance matrix, P, can be then updated using the two stage discrete time Kalman filter as follows [62]

- Prediction stage:

$$\begin{aligned} x_k^- &= Ax_{k-1} + Bu_{k-1} \\ P_k^- &= AP_{k-1}A^T + Q \end{aligned} \tag{5.21}$$

- Update stage:

$$\begin{aligned} K_k &= P_k^- H^T [HP_k^- H^T + R]^{-1} \\ y_k &= [z_k - Hx_k^-] \\ x_k &= x_k^- + K_k y_k \\ P_k &= P_k^- - K_k H P_k^- \end{aligned} \tag{5.22}$$

where K is the Kalman gain and y is referred to as the innovation process. In each iteration, in the prediction stage, states and their covariance evolve based on the model derived from the bioheat partial differential equation. The control input can be determined based on the heat excitation field which is the received HIFU intensity at he focus in our case. In the update stage the innovation process is used as the correction term weighted by the Kalman gain K. The innovation process can be considered as a measure of error between the prediction and the measurements.

5.2.4 Frame Rate Dependent Temporal Accumulation

In the non-model based techniques, in order to map the frame to frame temperature changes resulting from the temperature reconstruction filter to the absolute temperature a temporal accumulation is always required. This process, however, is usually performed without taking the frame rate dependency of the temperature changes into account which sometimes results in erroneous temperature rise and fall slopes. The model based technique based on the Kalman filter formulation presented here, incorporates the frame rate dependency through the discretization of the model imposed by the bioheat equation. This way, changes in the frame rate will directly affect the temporal features of the estimated temperature based on the bioheat dynamic.

5.2.5 Artifact Reduction Using Kalman Filter

The main assumption behind the Kalman filter derivation is a Gaussian distribution model for states, model and measurement noises. This assumption, however, is not completely valid as the temperature reconstructed based on the *in vivo* displacement data can be significantly distorted by the mechanical strains due to natural motions. In case of small localized deformations, these motions can create artifacts in the estimated temperature. In more sever cases, out of plain motions and complete deformation of the diffused scattering medium can occur which in turn can lead to speckle tracking failure. These events can be modeled as highly colored disturbances in the linear estimation model. However, the two stage setup implied by the Kalman filter, provides the ability to turn off the update stage whenever the measurements are largely contaminated by the artifacts or the displacement tracking fails. An artifact moment detection mechanism is required which can detect such time duration. After detection of such time intervals the estimated temperature dynamic evolves based on the state-space model derived from the bioheat equation in a predictive manner.

Artifact Event Detection

Successful implementation of the prediction based approach requires accurate estimation of the motion moments. Depending on the post processing requirement in terms of real-time implementation or post treatment assessment these methods can be categorized into two major categories:

1. **Real-time (casual) methods**: In these methods motion artifact moments are detected either by tracking the cross correlation values from the speckle tracking algorithm or by observing the artifactual temperatures field outside the heated region. The latter is usually practical when motion artifacts are not causing speckle tracking failure while the former can be used for large scale motions and deformations which can lead to speckle decorrelation and displacement tracking failure. Hence, real-time methods can be categorized as follows

   (a) Large scale motions: During large motions, speckle tracking algorithm may fail due to strong decorrelation of the speckle patterns. Using the magnitude

of the frame to frame cross correlation explained in chapter 3 these events can be detected using a thresholding method.

(b) Small scale motions: The normalized Euclidean norm of the two dimensional temperature reconstruction filter output matrix outside the target region can be used to detect non-thermal events such as breathing and gasping motions. This measure is defined as

$$\xi = \frac{\|\theta_a\|}{MN} \tag{5.23}$$

where θ_a is the artifactual estimated temperature outside the heated region and M and N are the dimensions in the axial and lateral directions correspondingly.

(c) External inertial sensors can also be used to detect and reject the data during large motion intervals

The requirement for all cases is a delay in commanding the Kalman filter such that the events can be prevented without disrupting the true temperature profile. It should be noted that as the measurement data is the temperature rate (not the absolute temperature) any instantaneous artifact can create a permanent bias in the estimated temperature due to lack of a direct measurement. This class of motion detection instances is suitable for both monitoring and control as the amount of lag can be kept within a time interval during which temperature change is minimal. This is specially practical since our imaging system works at relatively high frame rates (approximately 100 frames per seconds).

2. **Non Real-time (non-casual) methods**: In these methods, the goal is to enhance the estimated temperature field retrospectively. Hence they are not suitable for real-time monitoring and/or control of the therapy procedure but they can be used for offline assessment of the therapy.

Chapter 6

Adaptive and Model Based Techniques: Experimental Results

We present the results of using the adaptive and model based techniques for *in vivo* ultrasound temperature estimation. The adaptive technique discussed in the previous chapter will be used for reducing gasping artifacts occurred during *in vivo* temperature tracking of the subtherapeutic HIFU shots in the hind limb of the Copenhagen rats. We then present the results of applying the Kalman filter method on the data collected during heated wire phantom experiment described in chapter 4. The Kalman filter method will be then used for *in vivo* temperature estimation where it is combined with motion detection algorithms to detect prediction cycles.

6.1 Subtherapeutic Shots in The Hind Limb of Copenhagen Rats *In Vivo*

6.1.1 Material and Method

The M2D data was acquired at 40 MHz sampling rate and about 91 frames per second during subtherapeutic HIFU shots in the hind limb of a Copenhagen rat as described in [63]. The HIFU shots were created using a 64-element DMUA transducer (Imasonic, FR)

operating at 3.5 MHz as described in [64]. The M2D data was acquired using imaging pulses centered at 7.5 MHz and a linear array (HST 15-8, Ultrasonics, BC, CA) and as described in [41], which allowed for relatively high frame rates at the expense of smaller lateral extent of the image. The animal was partially submerged in a temperature controlled (34°C) degassed water and anesthetized using Ketamine and Xylazine under University of Minnesota approved IACUC protocol. This combination often results in deep anesthesia which appear to change the breathing pattern of the animal. For example, the animal gasps for air at semi-regular intervals after each period of low breathing activity. These gasps are often separated by periods of 1.5 - 2 seconds and result in significant displacements and strains throughout the hind limb that present as temperature artifacts. Frame rates in the 80 - 200 frames per second range were found to be necessary for capturing the transients of tissue motion and deformation due to pulsation, breathing as well as the radiation force effects of the pulsed HIFU beams.

6.1.2 Data Processing

In all experiments the M2D data was collected before, during and after the heating procedure for use in calculating the incremental displacement using speckle tracking algorithm as presented in [38]. A kernel length of about 9λ (1.84 mm) was used for all experiments. The incremental displacement field was passed through the axial filter described in (2.15) with z_0= 6 mm. This value of z_0 provided best results when combined with the adaptive motion compensation technique. Temperature coefficients α and β were set to 3×10^{-4} °C^{-1} and 2×10^{-3} °C^{-1}, respectively based on the average values of thermal coefficients for soft tissue [52],[53]. The integrator part of the axial filter in (2.15) was also applied in the reverse direction to compensate for the group delay. After performing the axial processing, the data was passed through a frame-to-frame accumulator followed by a low-pass filer with the cut off frequency of 1.5 Hz to create the final estimated temperature. In each experiment, the baseline temperature was measured and used to map the estimated temperature rise to the absolute temperature.

Adaptive Filter

After applying the temperature reconstruction filters on the displacement data, mechanical deformation foci were observed throughout the imaging plane and one location was

selected using a simple threshold on the strain data . 33 points were then selected as the interference inputs to the algorithm. The deformation foci can occupy few millimeters in each direction in the imaging plane. Considering the axial-lateral resolution of our imaging system which was about $19\mu \times 200\mu$ this constitutes more than 100 samples in the axial and few samples in the lateral direction. At each location 11 points were selected axially at three A-lines which resulted in a total of 33 points. No significant improvement was observed by increasing the number of training points beyond this value. Classic Normalized Least Mean Square (NLMS) algorithm with the step size of $\mu = 0.5$ was implemented on the artifactual (before HIFU was applied) temperature data to train the coefficients of the filter for each grid point in the target region. This value of μ guarantees the convergence of the NMLS algorithm [3][1] . The update process stopped once the artifactual temperature dropped below 38°C where the baseline temperature was 34°C.

Kalman Filter

The set of state space equations in (5.8) can be defined using the tissue dependent thermal coefficients ϵ and γ. However we will only need the value of γ as we will exclude the control input source P in the final implementation. The thermal diffusivity D was set to $0.11 \times 10^{-6} m^2/s$ based on its average value in soft tissue [52]. This value was also used for the tissue mimicking phantom. The speed of sound was set to 1550 m/s which resulted in an axial resolution of about 19 μm based on the 40 MHz sampling rate of the RF data. The axial resolution also defines the Δz in (5.6). These values of Δz and D resulted in a γ of 293.03 1/s.

(a) **Initialization**

A grid of 400 points in the axial direction was chosen such that the approximate focus was around the middle point. There were two state variables per grid point in which the 800×800 process noise covariance matrix was modeled as a diagonal

[1] A $0 < \mu < 2$ results in a stable NLMS algorithm

matrix as

$$Q = \begin{pmatrix} 10^{-3} & & & \\ & 5 \times 10^{-3} & & 0 \\ & & \ddots & \\ & 0 & & 10^{-3} \\ & & & & 5 \times 10^{-3} \end{pmatrix} \tag{6.1}$$

The 800×800 state covariance matrix was set to

$$P = \begin{pmatrix} 10^{-3} & & & \\ & 10^{-1} & & 0 \\ & & \ddots & \\ & 0 & & 10^{-3} \\ & & & & 10^{-1} \end{pmatrix} \tag{6.2}$$

The 400×400 measurement noise covariance matrix was set to

$$R = \begin{pmatrix} 10^{-1} & & & \\ & 10^{-1} & & 0 \\ & & \ddots & \\ & 0 & & 10^{-1} \\ & & & & 10^{-1} \end{pmatrix} \tag{6.3}$$

These values of Q, P and R matrices were chosen experimentally such that resulting bias during update and prediction was minimized. The algorithm started with assigning baseline temperature to all temperature state variables and zero values to the state corresponding to the temperature rate.

(b) **Measurement**

The frame to frame temperature changes were used as the measurement at each grid point. The same data was also passed through a band limited accumulator formed by an ideal accumulator followed by a 1.5 Hz bandwidth low pass filter to form the conventional temperature estimates.

(c) **Artifact Event Detection**

The normalized Euclidean norm of the two dimensional temperature outside the target region ξ based on (5.23) was used to detect the large motion events. The region constituted 3 first and 3 last A-lines in the M2D tracking plane. A threshold of 0.05 was used to detect the events. The event intervals were then applied to turn off the update step of the Kalman filter with different time sample lag values where a lag of 15 was found optimal. This value of lag was determined experimentally to maintain the maximum temperature build up less than 1.5 °C and early turn off of the update step to obtain the best prediction results.

(d) **Prediction, Update and Control Input**

The Kalman iterations were performed for each A-line in the axial and temporal directions and proceeded to the next A-line. We excluded the use of 2-D filtering to emphasis on the smoothing offered by the model based derivation based on the Kalman filtering. At each iteration the state variables corresponding to a large motion area skipped the update step while other states allowed for update using the corresponding measurement data. We excluded the use of control input u in (5.11) due to lack of accurate *in situ* measurement of the HIFU intensity at the focus.

6.2 Adaptive Filter Results

We present the results of applying subtherapeutic HIFU shots in the hind limb of a Copenhagen rats *in vivo*. Subtherapeutic HIFU started after one second of baseline measurements and was on for 750 ms. The total duration of data recording was 4 seconds where sporadic gasps occurred within the data collection interval.

Subtherapeutic HIFU Before Lesion Formation

Before forming a lesion, HIFU shots at subtherapeutic levels were delivered. During data collection three gasps occurred that caused major distortion in the estimated temperature field. Fig. (6.1) shows the artifactual temperature from few selected training points. As it can be seen the gasping has created three distinct peaks in a quasi periodic manner. A negative shift of about 0.5 $^{\circ}C$ is observed during the HIFU operation

which can be attributed to the acoustic radiation force. This mechanical effect appears throughout the converging region of the HIFU beam. It is important to select the training points that only capture the motion dynamic as other sources of interference like acoustic radiation force are not stationary processes and will cause bias during update phase. To avoid this effect, the training points are selected outside the converging region of the HIFU beam based on the pre-assessment of the transducer pattern.

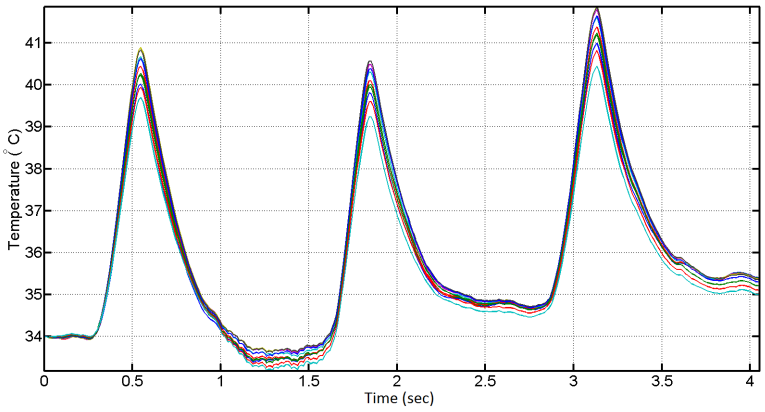

Figure 6.1: Artifactual temperature profiles used as the input data for training the adaptive filter motion compensation coefficients.

Fig. (6.2) shows the axial-lateral distribution of the estimated temperature field where (a), (b) and (c) are three gasping instances before and (d), (e) and (f) are the equivalent profiles after applying the adaptive motion compensation. As it can be seen the gasps have created artifacts which are spatially present in almost entire imaging plane. The adaptive filter has effectively reduced most of the these artifacts such that the heated spot is spatially distinct and identifiable at about 40 mm axial and 6 mm lateral location.

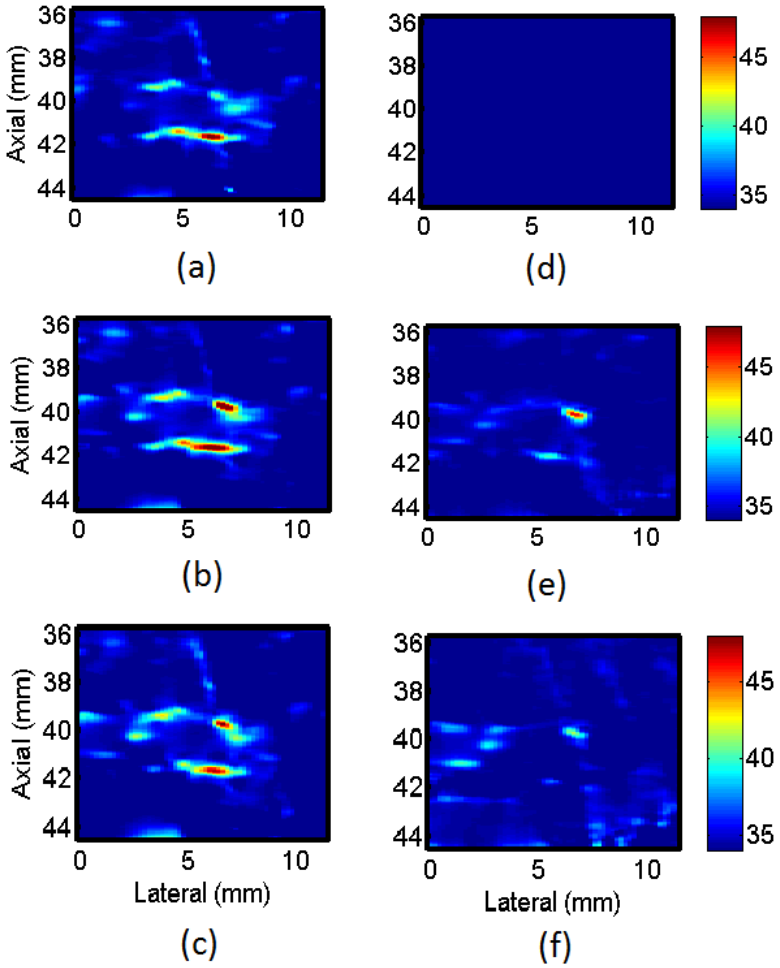

Figure 6.2: Axial-lateral distribution of the estimated temperature during subtherapeutic shots in the hind limb of a Copenhagen rat. (a), (b) and (c) three major gasp moments before motion compensation and (d), (e) and (f) after motion compensation.

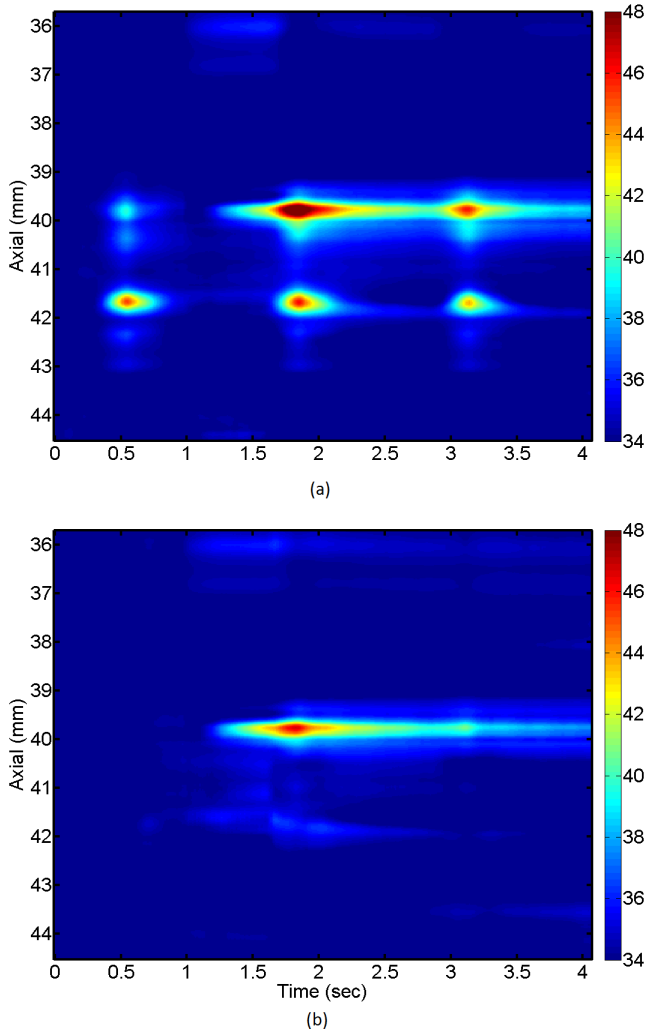

Figure 6.3: Axial-temporal distribution of the estimated temperature at an A-line close to the focus. (a) before motion compensation and (b) after motion compensation.

Fig. (6.3) shows the axial-temporal distribution of the estimated temperature profile before and after applying the motion compensation method. First of all, the spatial distribution of the temperature seems to be consistent with the focus of the HIFU beam which was at 40 mm. Ripple artifacts due to the thermal lens effect are considerably reduced by using the RESF model. In Fig. (6.3) (a) it can be seen that three strong gasps caused erroneous temperature estimates at three different time instances right at

the heating focus and 2 mm beyond the focus. The motion compensation method has successfully canceled the effect of these gasps without scarifying the spatial distribution of the temperature as it can be seen in Fig. (6.3) (b).

Fig. (6.4) shows the time profile of a point close to the focus. The NLMS algorithm is able to converge in a fraction of second. It is seen that while the corrected temperature preserves most of the unaffected parts of the temperature profile, large temperature errors in the order of $4°C$ (almost 40% of the peak temperature change) are corrected.

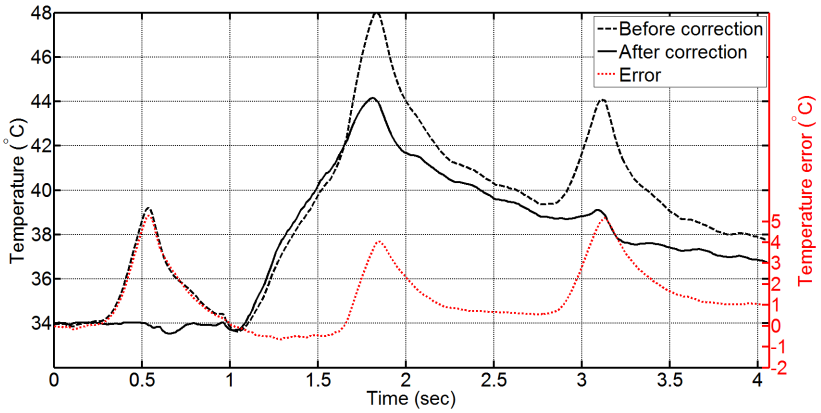

Figure 6.4: Temporal profile of the estimated temperature before (dashed black) and after (solid black) motion correction along with the difference (dotted red).

Subtherapeutic HIFU After Lesion Formation

After forming a lesion, subtherapeutic HIFU was delivered in the same location as the previous case and the temperature reconstruction filters were applied on the displacement data. Fig. (6.5) shows the temporal profile of the sample points used for training the motion compensation algorithm in this case. As it can be seen three major gasps can be identified with the first one that occurred just before the HIFU started at t =1 sec.

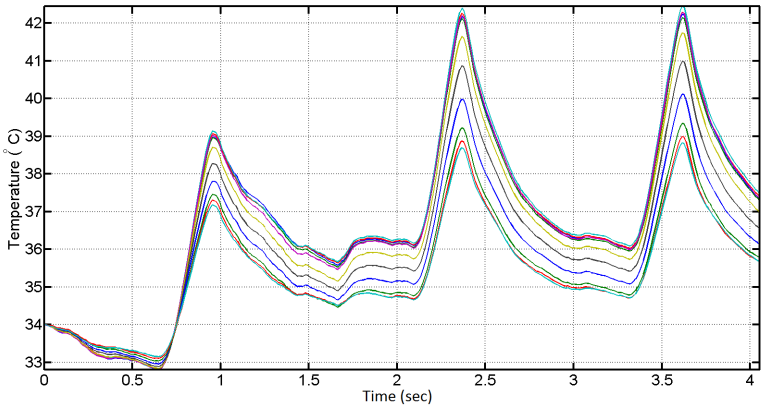

Figure 6.5: Artifactual temperature profiles used as the input data for training the adaptive filter motion compensation coefficients (subtherapeutic shot after lesion formation).

Fig. (6.6) shows the axial-lateral distribution of the estimated temperature field where (a), (b) and (c) are three gasping instances before and (d), (e) and (f) are the equivalent profiles after applying the adaptive motion compensation. All three gasps are effectively reduced by the adaptive motion compensation algorithm. This can be especially seen in Fig. (6.6)(c) and (f) where a major gasp overwhelmed the temperature estimation during the cool off cycle (after HIFU off) and the correction has greatly improved the spatial distribution of the temperature which is consistent with the previous time frames.

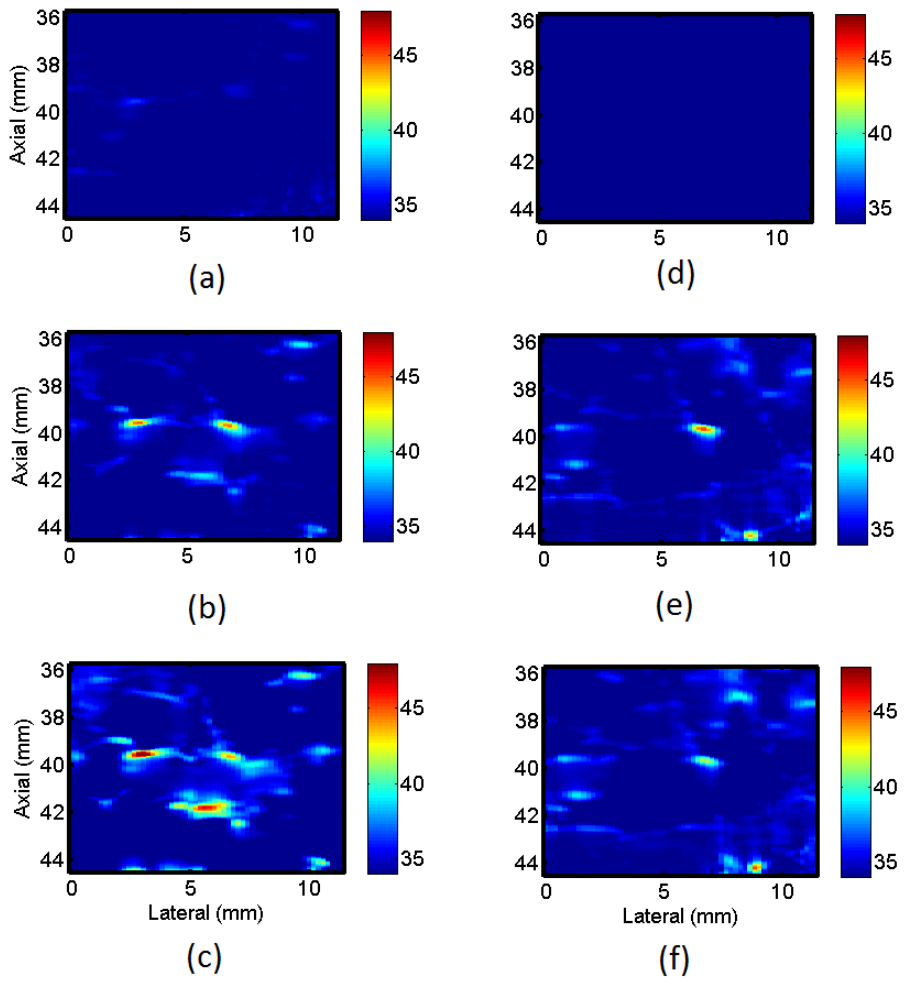

Figure 6.6: Axial-lateral distribution of the estimated temperature during subtherapeutic shots in the hind limb of a Copenhagen rat (after lesion formation). (a), (b) and (c) three major gasp moments before motion compensation and (d), (e) and (f) after motion compensation.

Fig. (6.7) shows the axial-temporal profile of the estimated temperature before and after applying the motion compensation method. The lateral point is selected near the temperature peak. Again the motion correction method has created a more consistent spatio-temporal temperature distribution.

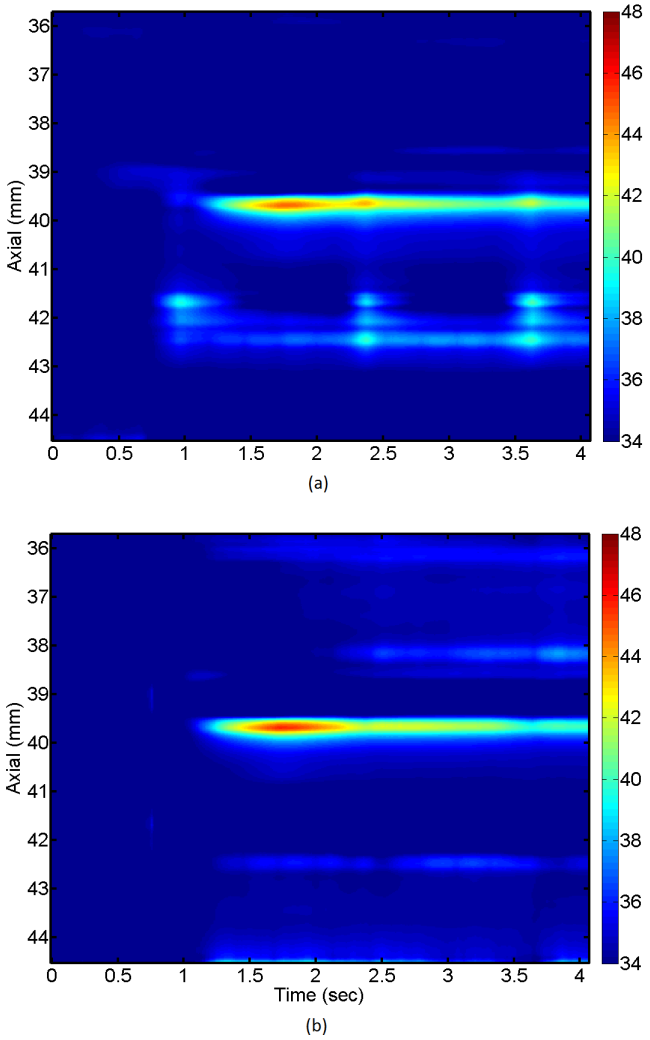

Figure 6.7: Axial-temporal distribution of the estimated temperature at an A-line close to the focus (after lesion formation). (a) before motion compensation and (b) after motion compensation.

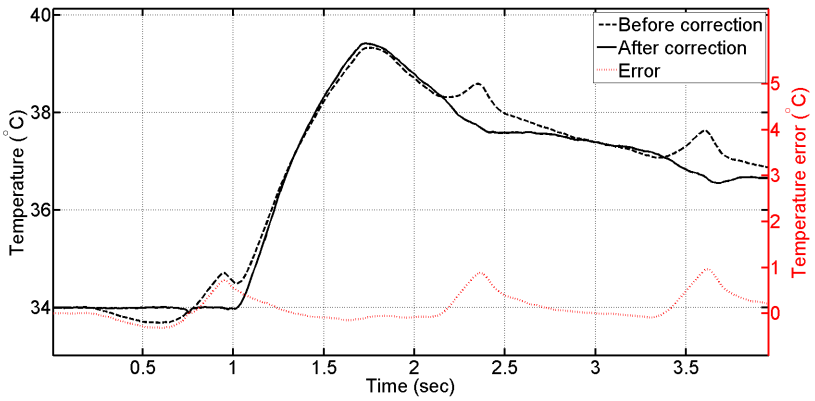

Figure 6.8: Temporal profile of the estimated temperature before (dashed black) and after (solid black) motion correction along with the difference (dotted red).

Fig. (6.8) shows the temporal profile of a point close to the focus. As it can be seen the adaptive technique has greatly improved temporal profile of the estimated temperature close to the HIFU start at $t = 1$ sec. The gasp artifacts are not very severe in this case where the difference between two results is less than $1°C$.

A Low Signal-to-Noise Ratio Case

This experiment was performed on the different leg of the same animal as in two cases presented above. Low RF data signal-to-noise ratio (SNR) in this case resulted in higher displacement tracking noise and hence less accurate temperature tracking. Fig. (6.9) shows the selected training points where the artifactual temperature maximum reaches about 37.5 °C. For this reason we selected 36 °C as motion foci detection threshold.

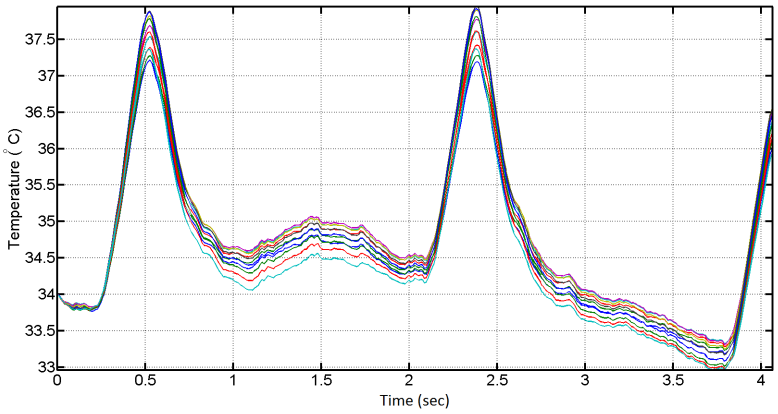

Figure 6.9: Temporal profile of the sample training points used for updating adaptive filter coefficients (low SNR case).

Fig. (6.10) shows the spatial distribution of the estimated temperature ate three time instances before (a), (b) and (c) and after (d), (e) and (f) after applying the motion compensation algorithm. The heated focus can be identified at around 45 mm axially and 8 mm laterally which shows 5 mm offset from the expected focus of the 40 mm based on the HIFU array geometry. This offset can be related to the beam aberration due to the heterogeneity of the medium and also wrong assumption about speed of sound in the imaging beamforming. Nevertheless, the adaptive method has been able to remove most of the artifactual temperature due to motion as it can be seen in Fig. (6.10) (a),(d) and also (c),(f). The negative temperature due to a gasp has completely diminished the true temperature as seen in Fig. (6.10) (c). Most of the temperature profile has been recovered by the motion compensation method in (6.10) (f) with effective cancellation of gasp artifacts in the surrounding area.

Fig. (6.11) presents the axial-temporal profile at an A-line close to the temperature peak before and after the motion compensation algorithm. As it can be seen in Fig. (6.11) (a) there is an interruption in the temperature tracking due to motion at around $t = 2.5$ sec. This is mostly recovered by the adaptive method as it can be seen in Fig. (6.11) (b).

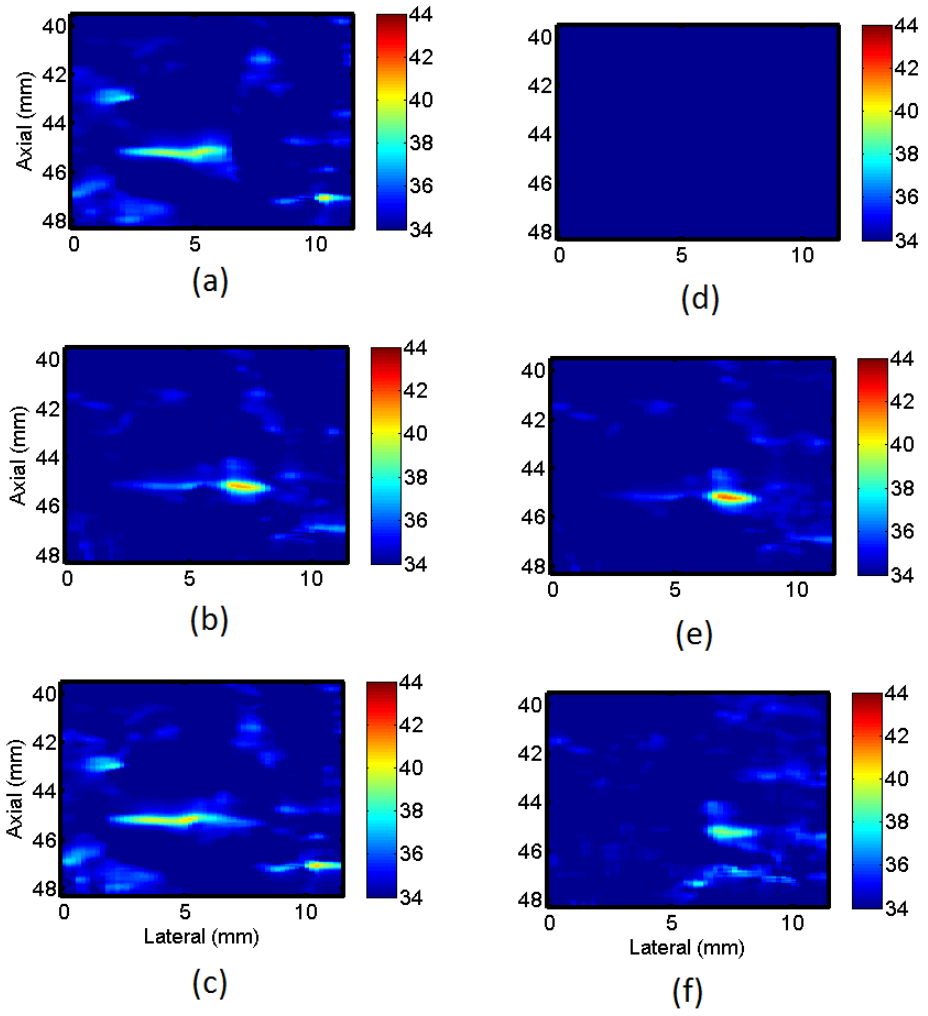

Figure 6.10: Axial-lateral distribution of the estimated temperature during subtherapeutic shots in the hind limb of a Copenhagen rat (low SNR case). (a) and (c) show two major gasps before motion compensation and (d), (f) the corresponding profiles after motion compensation respectively. (b) and (e) show the temperature profile at maximum temperature change in two methods.

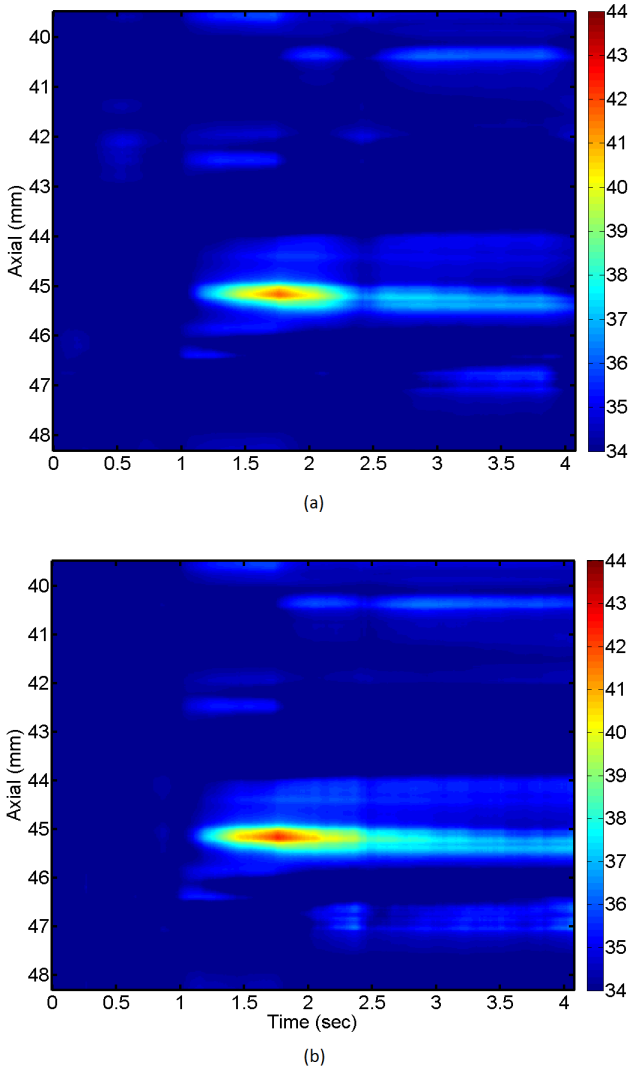

Figure 6.11: Axial-temporal distribution of the estimated temperature at an A-line close to the focus (low SNR case). (a) before motion compensation and (b) after motion compensation.

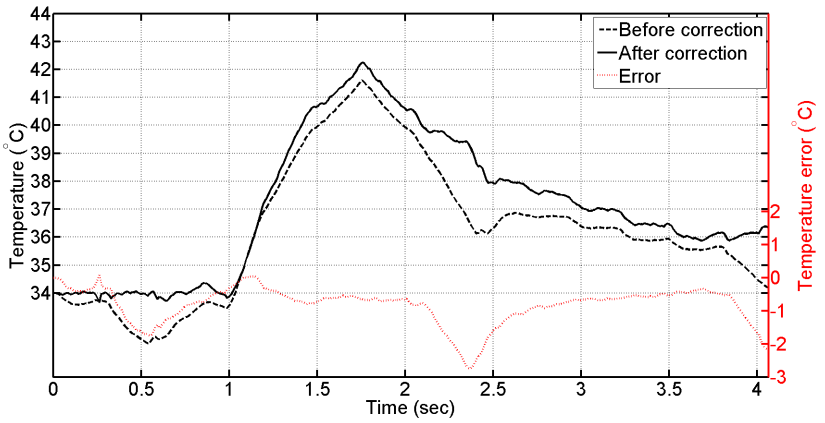

Figure 6.12: Temporal profile of the estimated temperature before (dashed black) and after (solid black) motion correction along with the difference (dotted red) (low SNR case).

Fig. (6.12) shows the time profile of a point close to the focus. The low SNR has resulted in a noisier temperature profile compared to the two previous cases. The motion compensation algorithm has been able to converge in a fraction of second and it has effectively canceled two motion errors occurred at $t = 0.5$ sec and $t = 2.3$ sec. A bias of 0.5 °C can be seen at peak temperature which can be related to the temporal change of motion artifact statistics. This can be also seen in Fig. (6.9) where there is an elevation in the temporal profile of the training points.

6.3 Kalman Filter Results

6.3.1 Wire Phantom Results

To evaluate the performance and consistency of the model based temperature estimation method we present the results of the wire phantom experiment that was described in chapter 3. The frame to frame temperature estimate using the RSEF model was used as the measurement input for each grind point without any temporal accumulation. Fig. (6.13) shows the spatial distribution of the estimated temperature using the Kalman filter. The temperature profile is consistent with our previous results using the band limited temporal accumulator shown in the Fig.(3.4). Fig. (6.14) shows the temporal

profile of sample points using the RESF model followed by a band limited temporal accumulator and the Kalman filter. As it can be seen there is a strong agreement between two methods in term of temperature dynamic.

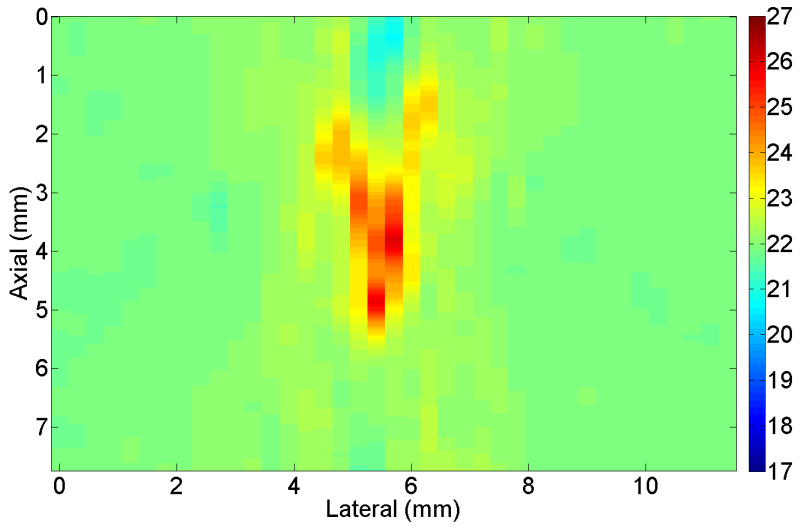

Figure 6.13: Axial-lateral distribution of the estimated temperature of the heated wire embedded in the tissue mimicking phantom at maximum temperature using Kalman filter.

Fig. (6.15) shows the axial distribution of the estimated temperature along an A-line close to the temperature peak for different values of diffusion coefficient D. It can be observed that larger values of D results in a smoother temperature as it is intuitively expected. Larger values of D offers a larger spatial dependency among adjacent points which in turn results in a low pass filtering in the axial direction.

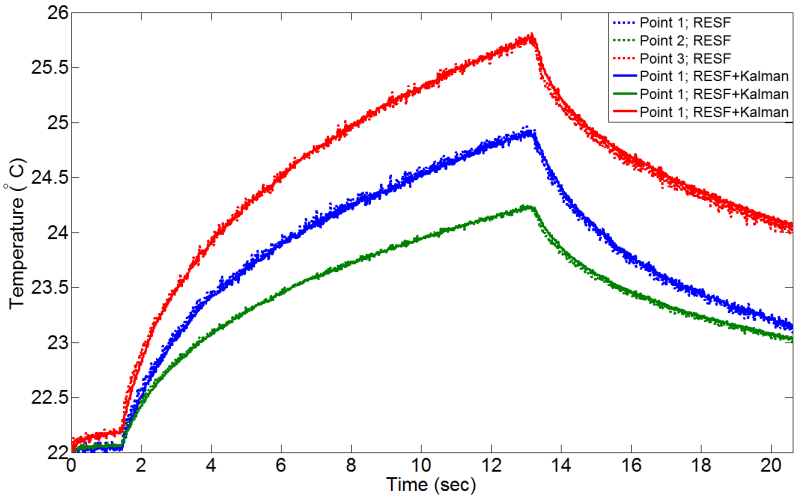

Figure 6.14: Temporal profile of the estimated temperature at sample points near the temperature maximum using (dotted) conventional (solid) Kalman filter.

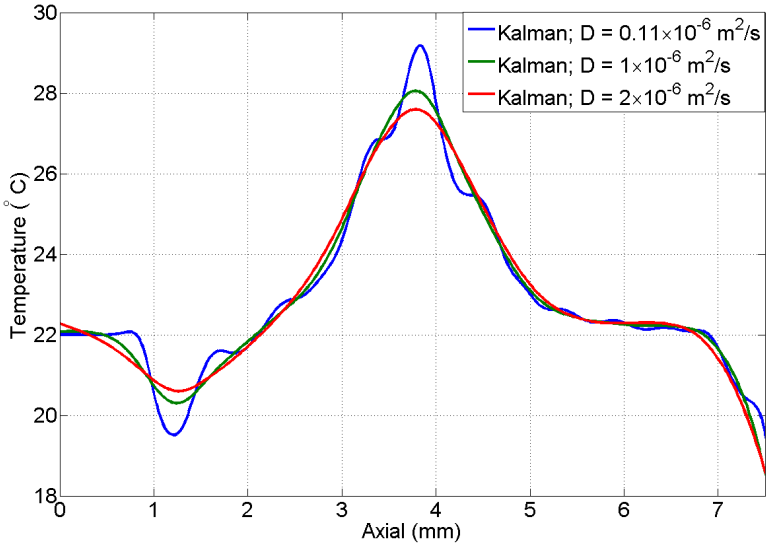

Figure 6.15: Axial distribution of the estimated temperature of the heated wire embedded in the tissue mimicking phantom at maximum temperature using Kalman filter with different values of diffusion coefficient D.

6.3.2 *In Vivo* Results

The performance of preliminary formulation of the Kalman filtering approach is illustrated using the same *in vivo* data described earlier in Sec. 6.2.

Subtherapeutic HIFU Before Lesion Formation

The data set that showed major gasps before, during and after applying the subtherapeutic HIFU was processed using the proposed Kalman filter technique. Fig. (6.16) shows the spatial distribution of the estimated temperature using the RESF model in (a), (b) and (c) and the corresponding Kalman filter results in (d), (e) and (f). These frames corresponded to three major gasping moments. As it can be seen the Kalman filter has resulted in a significant reduction of motion artifacts during second and third gasps. These results, however, are inferior to the adaptive filter results shown in Fig. (6.2) as some new artifacts are introduced which can be mostly related to noise build up during prediction cycles.

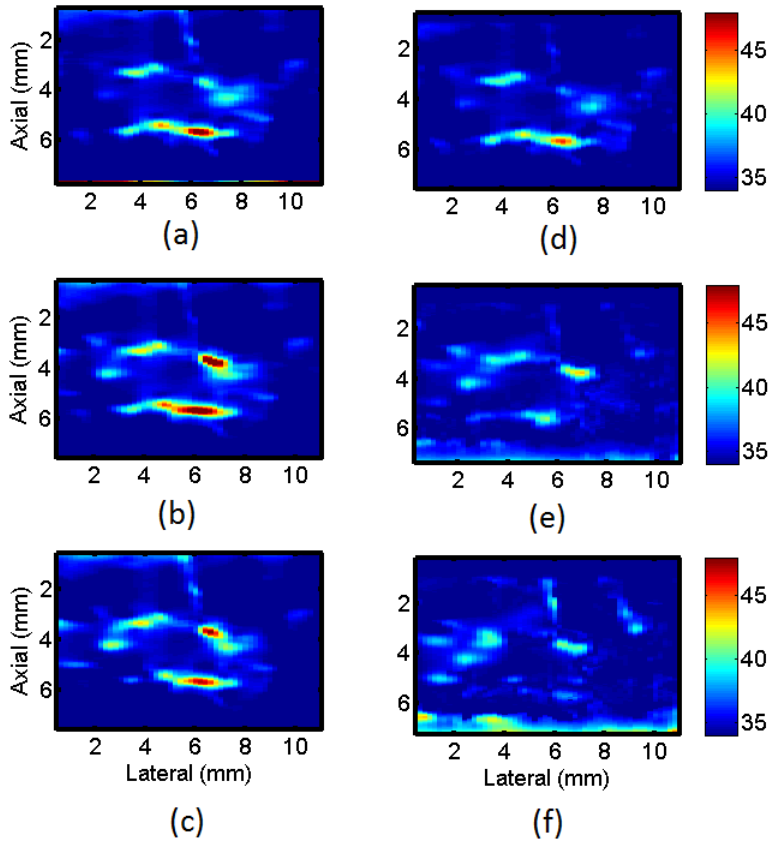

Figure 6.16: Axial-lateral distribution of the estimated temperature during subtherapeutic shots in the hind limb of a Copenhagen rat. (a),(b) and (c) three major gasp moments before motion compensation and (d),(e) and (f) after motion compensation using the Kalman filter.

Fig. (6.17) shows the axial-temporal profile of the estimated temperature before and after applying the Klaman filter. The motion artifacts which are seen in Fig. (6.17) (a) are mostly removed in Fig. (6.17) (b).

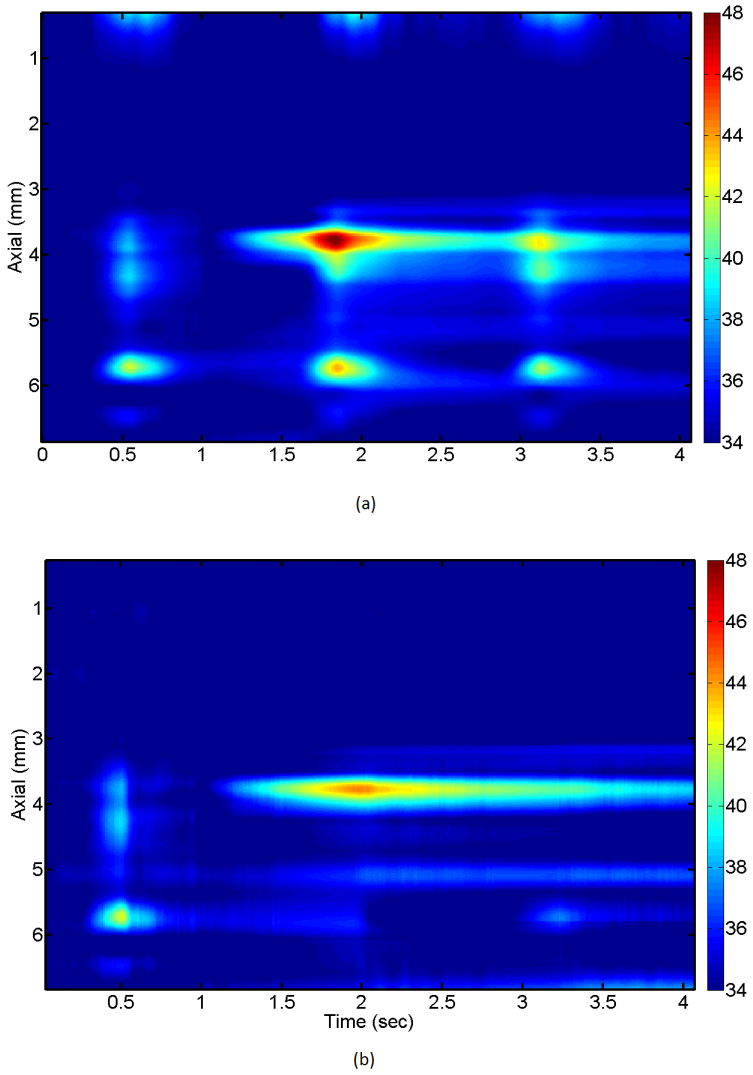

Figure 6.17: Axial-temporal distribution of the estimated temperature during subtherapeutic shots in the hind limb of a Copenhagen rat at a lateral location close to the heated spot. (a) before motion compensation and (b) after motion compensation using Kalman filter.

The temporal profile of the estimated temperature at the maximum temperature point is shown in Fig. (6.18) where the results of the adaptive and Kalman filters are also presented. The three different profiles correspond to (blue) uncorrected temperature,

(red) adaptive filter and (green) Kalman filter outputs. As it can be seen the Kalman filter has stopped updating the temperature profile based on the measurement during two time intervals $t = [1.5\ 1.75]$ sec and $t = [2.7\ 3.2]$ sec. During these intervals the states have been predicted based on the model imposed by state space transition matrix. This has created continuous tracking of the temperature in spite of large motion artifacts induced by gasping which is consistent with the dynamic of the bioheat equation. Since the measurement inputs to the Kalman filter are frame to frame temperature changes, any sudden bias will remain in the final estimate. This can be regarded as the main reason for the offset between the Kalman and adaptive filter outputs.

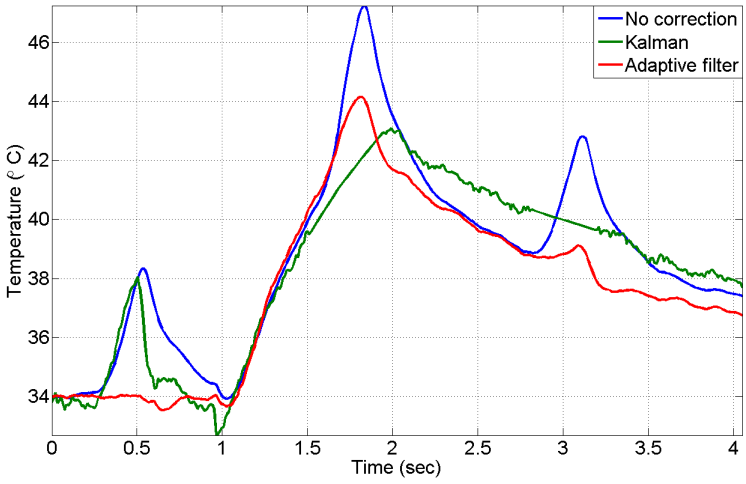

Figure 6.18: Temporal profile of the estimated temperature near the focus center during the subtherapeutic HIFU shots in the hind limb of the Copenhagen rat. (blue) uncorrected, (red) adaptive filter and (green) Kalman filter results.

Fig. (6.19) shows the difference between uncorrected temperature and the results of the adaptive and Kalman filters. As it can be seen both techniques have resulted in removing more than 4 °C artifactual temperature due to motion.

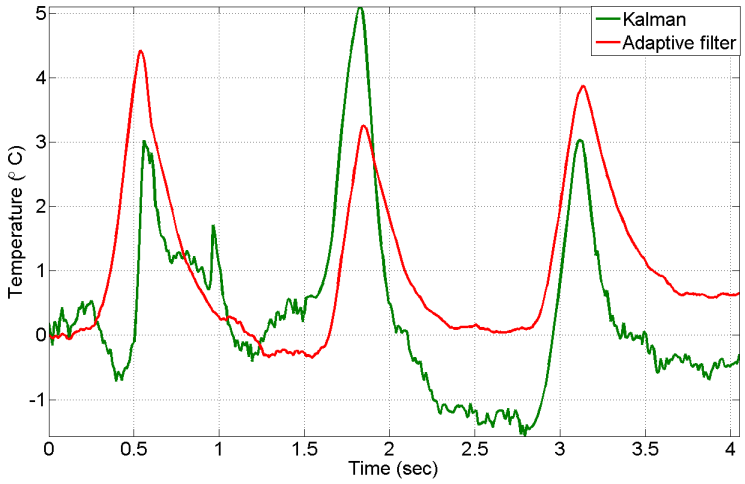

Figure 6.19: Differences between uncorrected temperature and the adaptive (red) and Kalman (green) filter outputs.

6.3.3 Effect of Different Lags

The motion event detection algorithm used the normalized norm of the two dimensional temperature reconstruction filter output outside the heated region, ξ, as the measure of motion. A command to the Kalman filter was generated whenever this value dropped below 0.05. The Kalman filter started using the corresponding measurement data with a time lag. Here we present the result of applying different lag values on the estimated temperature using Kalmnan filter.

Fig. (6.20) shows the estimated temperature at the center of the focus using different lag values and a threshold of 0.05. As it can be seen, a better estimate is achieved when using larger lag values. This is intuitively expected as the state bias due to the motion artifacts can be avoided at an earlier time. Due to the cumulative dynamic imposed by the state transition matrix this leads to a lower deviation from the true temperature.

Fig. (6.21) shows the corresponding differences between the uncorrected temperature profile and the Kalman output based on different lag values. It is expected that this difference to be small during time intervals that there is no motion artifact. The minimum value of this difference has occurred at lag of 15 which is also the optimal value

we have used throughout the Kalman filter results.

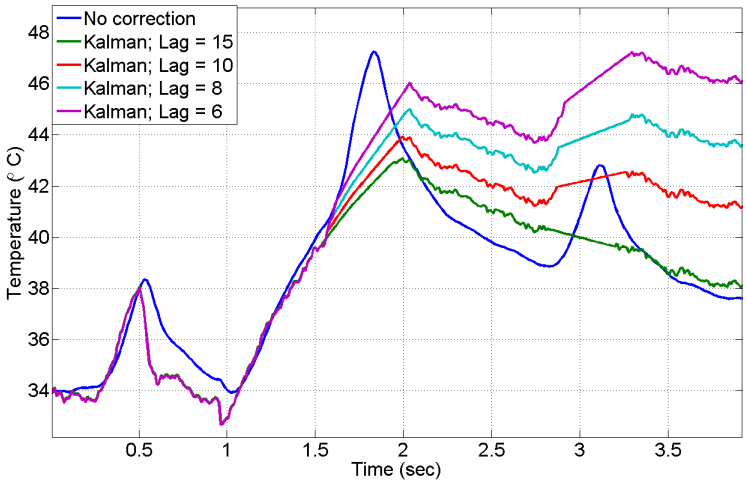

Figure 6.20: Temporal profile of the estimated temperature near the focus center using the Kalman filter with different lag values for the motion event command.

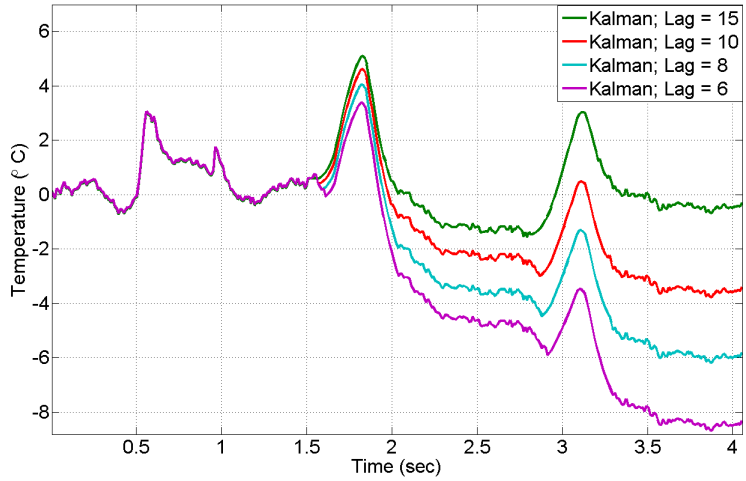

Figure 6.21: Difference between uncorrected estimated temperature and Kalman outputs for different lag values.

6.3.4 Effect of Different Thresholds

The motion event detection method used a threshold to declare a major motion event. To evaluate the effect of this variable on the performance of the artifact removal method based on the Kalman filter we present the results for different thresholds and constant lag value of 15. Fig. (6.22) shows the uncorrected temperature profile at a point close to the heating center along with the Kalman filter outputs for different threshold values. As it can be seen a larger threshold has resulted in a shorter pure prediction intervals. A small threshold ($\xi_{thr} = 0.02$) has caused longer prediction intervals which in turn has created larger deviation from the uncorrected temperature. A large threshold ($\xi_{thr} = 0.08$), on the other hand, has resulted in very short prediction intervals. This, in turn, has degraded the performance of Kalman filer prediction. This observation suggests an optimal threshold value of $\xi^*_{thr} = 0.05$ which has been used throughout the Kalman filter results.

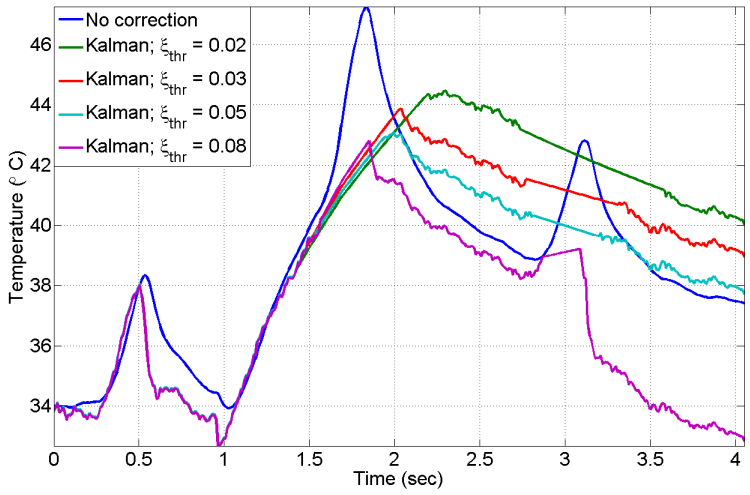

Figure 6.22: Temporal profile of the estimated temperature near the focus center using the Kalman filter with different threshold values on the normalized norm of the 2-D temperature reconstruction filter output.

Fig. (6.23) shows difference between the uncorrected and the Kalman filter output with different motion event detection threshold, ξ_{thr}. A threshold value of $\xi^*_{thr} = 0.05$

has resulted in the minimum deviation from the uncorrected temperature during no motion intervals.

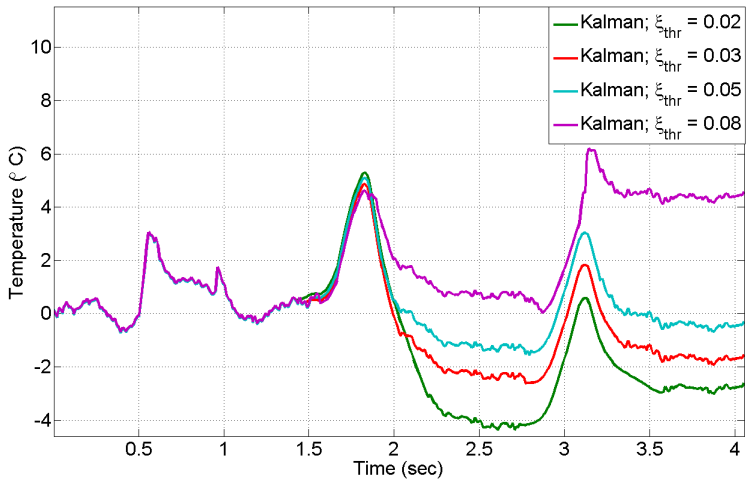

Figure 6.23: Difference between uncorrected estimated temperature and Kalman outputs for different threshold values.

A Low Signal-to-Noise Ratio Case

At high SNR, the Kalman prediction method showed good performance in removing motion artifacts with minor addition of prediction artifacts. At low SNRs, however, the residual noise on state variables might degrade the performance of the prediction step as the values of the state variables are biased prior to the prediction. We present the results of applying the Kalman filter for removing the motion artifacts during subtherapeutic HIFU in the hind limb of the Copenhagen rat where HIFU is deeply located in tissue and SNR is poor.

Fig. (6.24) shows the axial-lateral distribution of the estimated temperature using the conventional temperature reconstruction filter in (a), (b) and (c) and the corresponding Kalamn outputs in (d), (e) and (f) in three time instances. The artifact due to first gasp in Fig. (6.24) (a) is completely removed by the Kalman filter in Fig. (6.24) (d). Fig. (6.24) (b) and (e) show the distinct heated region around 4 mm axially and 7 mm laterally at similar temperature range. In Fig. (6.24) (a) and (c) two major gasps

occurred that are effectively removed by the Kalman filter in (d) and (f) respectively. This is especially interesting as the focused heating identified around (4mm,7mm) location is completely diminished during the second gasp and the Kalman prediction has been able to recover most of the temperature field as seen in Fig. (6.24) (e). The low SNR in all instances, however, has created some artifacts due to noise build up during prediction cycles.

The spatio-temporal profile of the estimated temperature at a lateral location close to the focus is shown in Fig. (6.25) where (a) is the uncorrected estimated and (b) is the Kalman filter output. As it can be seen there is an interruption in the uncorrected temperature profile estimate around $t = 2.5$ sec which has been mostly recovered by the Kalman filter. On the other hand, an artifacual temperature trace is seen 2 mm below the heated spot which can be related to the noise build up during the prediction cycles.

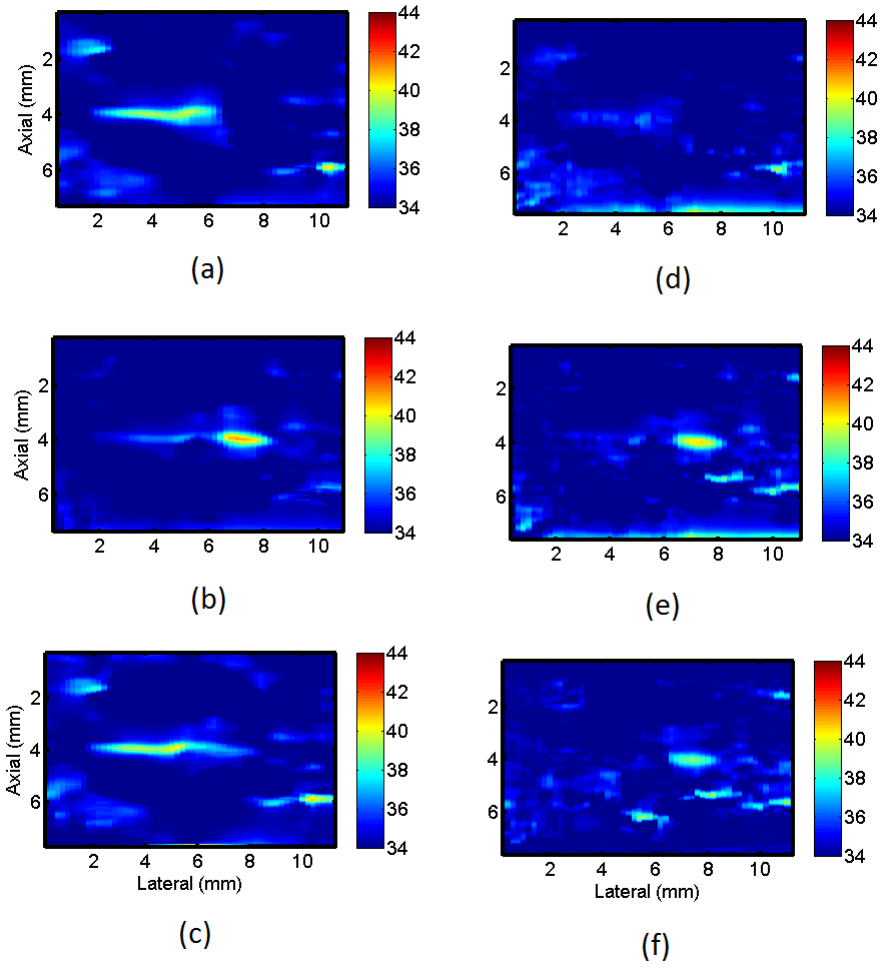

Figure 6.24: Axial-lateral distribution of the estimated temperature during subtherapeutic shots in the hind limb of a Copenhagen rat (low SNR case). (a),(b) and (c) three time instances using the conventional temperature reconstruction filter, and (d),(e) and (f) after motion compensation using the Kalman filter.

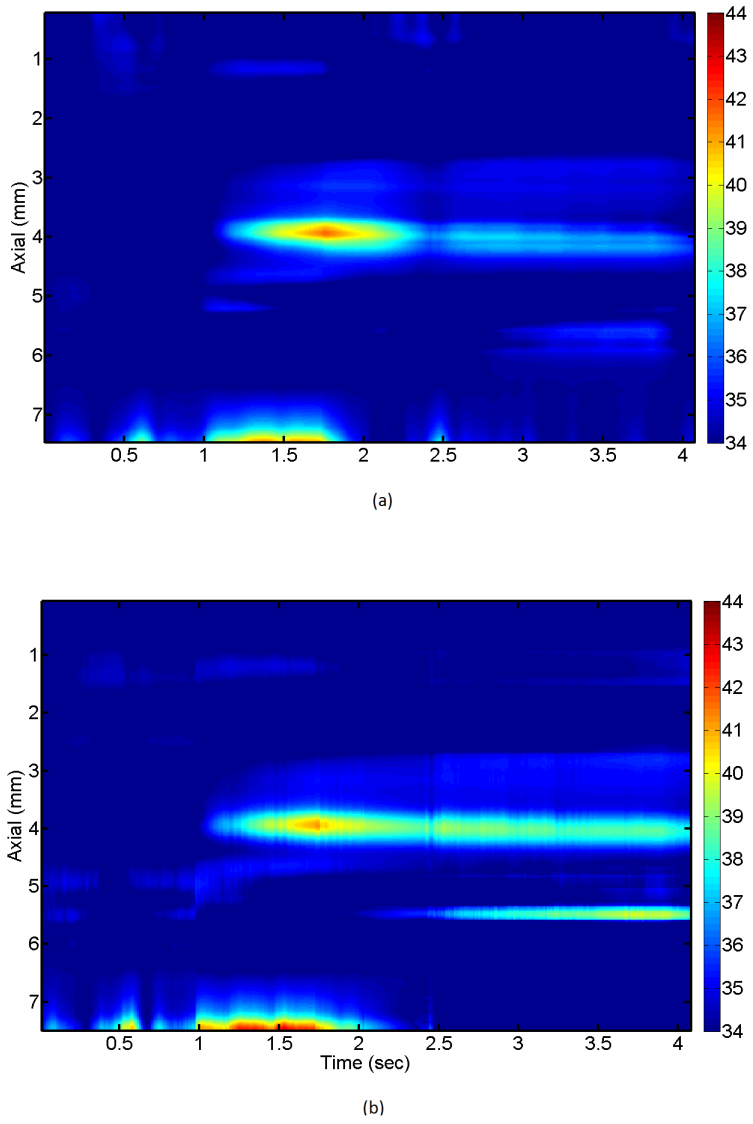

Figure 6.25: Axial-temporal distribution of the estimated temperature during subtherapeutic shots in the hind limb of a Copenhagen rat at a lateral location close to the heated spot (low SNR case). (a) before motion compensation and (b) after motion compensation using Kalman filter.

Fig. (6.26) shows a temporal profile at a point close to the heated center. The results show uncorrected temperature (blue), adaptive filter corrected (red) and Kalman filter

corrected (green) profiles. As it can be seen the Kalman filter result is in good agreement during absence of the motion artifacts while adaptive filter has shows a bias. This bias was shown to be due to the effect of acoustic radiation force on the training point profiles.

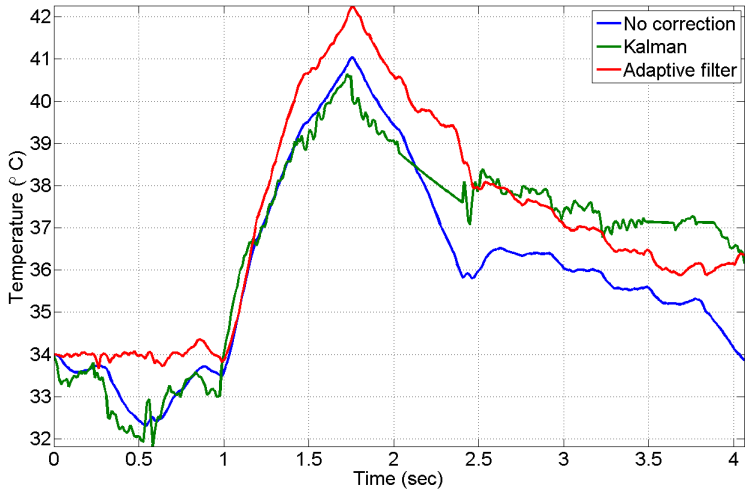

Figure 6.26: Temporal profile of the uncorrected temperature (blue), Kalman filter corrected (green) and adaptive filter corrected (red) at point close to the heating focus during subtherapeutic shots in the hind limb of a Copenhagen rat (low SNR case).

Fig. (6.27) shows the difference between the uncorrected temperature estimate and Kalman filter and adaptive filter outputs. Both corrected methods show removal of the motion artifacts while Kalman has resulted in less bias before occurring the second gasp.

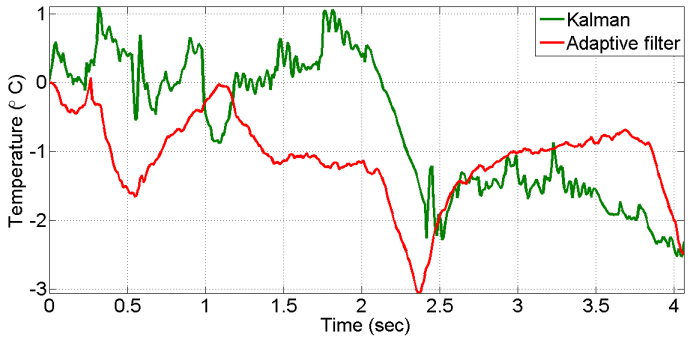

Figure 6.27: Temporal profile of the difference between the uncorrected temperature and Kalman filter (green) and adaptive filter (red) at point close to the heating focus during subtherapeutic shots in the hind limb of a Copenhagen rat (low SNR case).

6.4 Discussion and Conclusion

In this chapter we presented the results of using two different techniques in enhancing the *in vivo* ultrasound temperature estimation. We first presented a spatial adaptive filter for motion compensation. Using the quasi periodic nature and spatially global availability of the motion artifacts, we showed how an adaptive filter coefficients can be trained and used to remove the motion artifacts using the information from outside the heated region. It was shown that the corrected temperature estimate maintained most of the spatial and temporal features of the expected temperature profile, a feature which can not be achieved by using ordinary selective filters. We presented three *in vivo* cases with different artifact patterns and signal conditions. All cases showed improvements after applying the spatial motion compensation adaptive filter. This demonstrates the applicability of the this technique for *in vivo* applications. Deviation from the quasi periodic assumption of the motion artifacts, such as those created by acoustic radiation force, were shown to adversely affect the performance of the adaptive method. The presence of the deformation foci was another key assumption which made this approach a good candidate. More complex deformation patterns may be seen in different organs or with different anesthetizing methods which may require more careful selection of the training points.

We also presented the results of the model-based technique for tracking of the temperature. In order to validate the reconstruction model implied by the Klaman filter we first presented phantom experiment results where a good spatial and temporal agreement was observed between the conventional and Kalmnan filter approaches. We also showed that the dependency of the output to the state space model through variations in the diffusion coefficient, D where the model imposed a spatial dependency among adjacent points based on the dynamics of the bioheat equation. In this case, the spatio-temporal state space model only accounted for interactions between neighboring points on an axial (1D spatial) grid without accounting for global motion. To do this, we have implemented a motion detection scheme based on normalized Euclidean as shown in (5.23). This measure, together with a time-lag parameter were used to control the behavior of the bioheat-based Kalman filter in the presence of motion artifact.

We presented the results of using Kalman filter with a constant diffusion parameters for two *in vivo* cases. The results demonstrate that using normalized Euclidean norm of the output of the conventional temperature reconstruction model the motion intervals can be detected. Upon exceeding a specified thresholds, commands from the motion detection were used to turn off the measurement update of the Kalman filter, leading to a pure prediction based on state transition matrix. The results were shown to be in good agreement with the uncorrected temperature during absence of the motion artifacts and effective in reducing them during the motion intervals. It was also highlighted the prediction model is sensitive to the noise and can create additional artifacts in low SNR situations.

The motion event detection was parameterized based on a threshold value and time lag between the event detection and Kalman filter update. The results demonstrate that the method is effective with various values of thresholds and time lags. However, the results also suggest that there is an optimal threshold value for which the deviation from the expected temperature estimate is minimum. This value was found experimentally. A lager time lag resulted in a better estimate. In temperature control applications, however, smaller time lags are desired to avoid over exposure to the therapy. A more accurate spatio-temporal model for deriving the Kalman filter equation is still needed.

Chapter 7

Conclusion and Future Work

In this thesis we investigated two main aspects of the echo shift based ultrasound temperature estimation problem. We first presented a new reconstruction model for ultrasound thermography using speckle tracking displacement. We then presented statistical signal processing techniques to improve the performance during *in vivo* ultrasound temperature estimation.

7.1 Temperature Estimation Model

7.1.1 Conclusion

RESF model for temperature reconstruction

The recursive echo strain filter (RESF) was presented as a new model for temperature reconstruction based on the displacement data. Instead of a wide band differentiator implied the widely used δ-ESF model, RESF model resulted in an inherent band limited differentiator in the spatial dimension via an integrator part in which the parameters were defined based on the local tissue properties. The improvement suggested by the RESF model was validated by careful experiments in tissue mimicking phantoms and *ex vivo* blocks of bovine hear tissue. The reconstruction model suggested by RESF was shown to appear as a differentiator-integrator in the axial direction with a simple digital filter realization. It was shown that to achieve similar results using the δ-ESF model, long axial filter is required which imposes further computational burden. The RESF

model also can allow for accounting for bi-directional displacement due to thermal expansion. We also presented a closed form solution of for the itegro-differential equation in the RESF derivation.

Modeling of ray aberration using ray tracing analysis

The ray aberration due to change in speed of sound was analyzed using a ray tracing model. A variational calculus approach was used to determine the ray trajectory passing through a highly heterogeneous speed of sound medium. The results of the simulation qualitatively confirmed the appearance of the ripple artifacts at and beyond the focus during experimental observation. However, no attempt was made to create quantitative relationship or inverting the effect of such artifact.

7.1.2 Future Work

The RESF model presented in this this thesis relies on good assumptions on the tissue dependent thermal properties. In a highly heterogeneous medium where the tissue content is spatially variant the scatterer motions can be highly complex. A full inverse scattering model which is capable of capturing scatterers' motions, both apparent due to variable speed of sound and physical due to thermal expansion, can be used for relating the displacement data to the real temperature change. Such model can be initialized by a pre-assessment of the underlying tissue using other imaging modalities with higher resolution such as MR. The scatteres' motion can be also used to predict the artifact pattern due to aberration using the proposed ray tracing model. Once the beam aberration model is known, inverse spatial filtering can be applied to the displacement data prior to the temperature reconstruction, similar to the correction technique used for correction of the spherical aberration of the Hubble telescope [65].

7.2 *In Vivo* Ultrasound Temperature Estimation

7.2.1 Conclusion

In the second half of this work we proposed two statistical signal processing approaches to mitigate the motion artifacts during *in vivo* ultrasound temperature estimation. It was shown such artifacts can not be simply removed using selective filters due to the wide range of shared bandwidth.

Adaptive motion compensation

We presented a motion compensation algorithm based on the adaptive filter technique with NLMS algorithm. The algorithm used deformation foci outside the heated region to train the filter coefficients. These coefficients were then used to remove the motion artifacts during tracking of subtherapeutic temperature changes in the hind limb of the Copenhagen rats *in vivo* . The results showed successful removal of artifacts induced by natural gasping motion with negligible effect on the expected temperature dynamic. The performance of the algorithm was based on the existence of the deformation foci outside the conversing region of the HIFU beam. This was especially important as we highlighted the effect of acoustic radiation force as a source of bias in the final output. For this reason it was emphasized that the training point must be selected outside the converging region of the HIFU beam. We showed the repeatability of this method by presenting three different *in vivo* cases where gaping motion occurred at different time instances and under different signal SNR.

Model based ultrasound temperature estimation

We presented a model based technique for tracking of temperature. The model was derived by direct discretization of the bioheat partial differential equation. We then presented a Kalman filter formulation based on the state space model. The performance of the temperature reconstruction based on the Kalman filter was validated using phantom experiment data. We then proposed an artifact removal algorithm based on the prediction model offered by the Kalamn filter formulation. An event detection method

based on the normalized Euclidean norm of the two dimensional artifactual temperature data was used to create prediction commands to Kalman filter. We then showed the results of using the proposed method on *in vivo* data sets where successful removal of the motion artifacts were presented. The performance of the algorithm, however, depends on careful selection of a threshold parameter and time lag. The effect of these parameters on the performance of the Kalman based motion artifact removal algorithm were highlighted. The spatio-temporal filtering offered by the model based techniques provided consistent temperature estimation based on the bioheat dynamic.

7.2.2 Future Work

The following are suggested as straightforward extension of the current work:

- The Kalman filter realization of the model based techniques presented in this thesis was implemented in one dimension. The model can be extended to higher dimensions in a straightforward manner by expanding the Laplacian term in (5.5). This may lead to a more computationally intensive implementation. However, sparse implementations such as ensemble Kalmnan filter can be used.

- We excluded the use of control input in the final implementation. However, an accurate model of the delivered acoustic energy can be used as the control input. The use of control input will improve both measurement update and pure prediction during motion cycles.

- We assumed a constant diffusion coefficient. This coefficient can be assumed spatially variable and be embedded in the state equations which will result in a nonlinear model. The problem can be solve using extended Kalman or particle filtering methods.

- The motion event detection process can be improved using a cyclostationary modeling.

In addition to the echo shift based ultrasound temperature estimation, the proposed model based method can be used with any other temperature measurement modality. This method can be also used in other applications involving partial differential modeling

of the physical properties with discrete samples. One such application of this method is tissue motion and elasticity imaging based on the Navier-Stokes' equation [66]

$$\rho\frac{\partial^2}{\partial t^2}\vec{u}(\vec{r},t) = (\bar{\lambda}+\bar{\mu})\nabla(\nabla.\vec{u}(\vec{r},t)) + \bar{\mu}\Delta\vec{u}(\vec{r},t) + \vec{f}(\vec{r},t) \tag{7.1}$$

where ρ is the local density of the medium, $\vec{u}(\vec{r},t)$ is the particle displacement field, $\bar{\lambda}$ and $\bar{\mu}$ are the bulk and shear modulus including viscosity and and $\vec{f}(\vec{r},t)$ is the external force field. Given the displacement data from the speckle tracking, it is possible to form the state space model in the similar way as presented in this thesis. The tissue viscoelasticity properties can be then estimated using a nonlinear estimator such as EKF or particle filtering.

References

[1] John R. Ballard. *Refocusing of Dual-mode Ultrasound Arrays for Optimal Therapeutic Gain*. PhD thesis, University of Minnesota, 2012.

[2] J.C. Bamber and C.R. Hill. Ultrasonic attenuation and propagation speed in mammalian tissues as a function of temperature. *Ultrasound in Medicine and Biology*, 5(2):149 – 157, 1979.

[3] Simon Haykin. *Adaptive Filter Theory*. Printice-Hall Information and System Science Series, 2002.

[4] Chris J. Diederich. Thermal ablation and high-temperature thermal therapy: Overview of technology and clinical implementation. *International Journal of Hyperthermia*, 21(8):745–753, 2005. PMID: 16338857.

[5] R Catane, A Beck, Y Inbar, T Rabin, N Shabshin, S Hengst, RM Pfeffer, A Hanannel, O Dogadkin, B Liberman, and D Kopelman. Mr-guided focused ultrasound surgery (mrgfus) for the palliation of pain in patients with bone metastases–preliminary clinical experience. 18(1):163–167, 2007.

[6] Elizabeth A. Stewart, Wladyslaw M.W. Gedroyc, Clare M.C. Tempany, Bradley J. Quade, Yael Inbar, Tilman Ehrenstein, Asher Shushan, Jonathan T. Hindley, Robert D. Goldin, Matthias David, Miri Sklair, and Jaron Rabinovici. Focused ultrasound treatment of uterine fibroid tumors: Safety and feasibility of a noninvasive thermoablative technique. *American Journal of Obstetrics and Gynecology*, 189(1):48 – 54, 2003.

[7] Mark La Meir. Surgical options for treatment of atrial fibrillation. *Annals of Cardiothoracic Surgery*, 3(1), 2014.

[8] Avi Schroeder, Joseph Kost, and Yechezkel Barenholz. Ultrasound, liposomes, and drug delivery: principles for using ultrasound to control the release of drugs from liposomes. *Chemistry and Physics of Lipids*, 162(1 - 2):1 – 16, 2009.

[9] Elizabeth A. Stewart, Jaron Rabinovici, Clare M.C. Tempany, Yael Inbar, Leslie Regan, Bobbie Gastout, Gina Hesley, Hyun S. Kim, Suzanne Hengst, and Wladyslaw M. Gedroye. Clinical outcomes of focused ultrasound surgery for the treatment of uterine fibroids. *Fertility and Sterility*, 85(1):22 – 29, 2006.

[10] S. Thomsen. Pathologic analysis of photothermal and photomechanical effects of laser-tissue interactions. *Photochemistry and photobiology*, 53(6):825–35, 1991.

[11] W. C. Dewey. Arrhenius relationships from the molecule and cell to the clinic. *International Journal of Hyperthermia*, 25(1):3–20, 2009.

[12] Eduardo Moros, editor. *Physics of Thermal Therapy: Fundamentals and Clinical Applications*. Taylor and Francis, Boca Raton, FL, 2012.

[13] Jing Chen, Bruce L. Daniel, and Kim Butts Pauly. Investigation of proton density for measuring tissue temperature. *Journal of Magnetic Resonance Imaging*, 23(3):430–434, 2006.

[14] Viola Rieke and Kim Butts Pauly. Mr thermometry. *Journal of Magnetic Resonance Imaging*, 27(2):376–390, 2008.

[15] A. Abragam. *The Principles of Nuclear Magnetism*. International series of monographs on physics. Clarendon Press, 1961.

[16] Simon J. Graham, Michael J. Bronskill, and R. Mark Henkelman. Time and temperature dependence of mr parameters during thermal coagulation of ex vivo rabbit muscle. *Magnetic Resonance in Medicine*, 39(2):198–203, 1998.

[17] J. C. Hindman. Proton resonance shift of water in the gas and liquid states. *The Journal of Chemical Physics*, 44(12), 1966.

[18] Yasutoshi Ishihara, Arturo Calderon, Hidehiro Watanabe, Kazuya Okamoto, Yoshinori Suzuki, Kagayaki Kuroda, and Yutaka Suzuki. A precise and fast temperature mapping using water proton chemical shift. *Magnetic Resonance in Medicine*, 34(6):814–823, 1995.

[19] B. Denis de Senneville, B. Quesson, and C. T. W. Moonen. Magnetic resonance temperature imaging. *International Journal of Hyperthermia*, 21(6):515–531, 2005.

[20] S.J. Graham, G.J. Stanisz, A. Kecojevic, M.J. Bronskill, and R.M. Henkelman. Analysis of changes in mr properties of tissues after heat treatment. *Magnetic Resonance in Medicine*, 42(6):1061–1071, 1999.

[21] Alan R. Bleier, Ferenc A. Jolesz, Mark S. Cohen, Robert M. Weisskoff, Julianne J. Dalcanton, Nobuya Higuchi, David A. Feinberg, Bruce R. Rosen, Robert C. McKinstry, and Stephen G. Hushek. Real-time magnetic resonance imaging of laser heat deposition in tissue. *Magnetic Resonance in Medicine*, 21(1):132–137, 1991.

[22] R. D. Watkins W. J. Adams J. F. Schenck R. H. Ettinger W. R. Freund J. P. Vetro H. E. Cline, K. Hynynen and F. A. Jolesz. Focused us system for mr imaging-guided tumor ablation. *Radiology*, 194:731–737, 1995.

[23] J. Jenne I. Simiantonakis R. Rastert H. J. Zabel P. Huber R. Bader C. Bohris, W. G. Schreiber and G. Brix. Quantitative mr temperature monitoring of high-intensity focused ultrasound therapy. *Magnetic Resonance Imaging*, 17:603–610, 1999.

[24] D. N. Smith P. E. Huber N. J. McDonnold J. Kettenbach J. Baum S. Singer K. Hynynen, O. Pomeroy and F. A. Jolesz. Mr imaging-guided focused ultrasound surgery of fibriadenomas in the breast: a feasibility study. *Radiology*, 219:176–185, 2001.

[25] R Seip, P VanBaren, C Simon, and E S Ebbini. Non-invasive spatio-temporal temperature change estimation using diagnostic ultrasound. In *Proc. IEEE Ultrason. Symp.*, volume 1, pages 1613–1616, 1995.

[26] A Nasiri Amini, E S Ebbini, and T Georgiou. Noninvasive estimation of tissue temperature via high-resolution spectral analysis techniques. *IEEE Trans. Biomedical Engineering*, 52(2):221–228, 2005.

[27] S. Ueno, M. Hashimoto, H. Fukukita, and T. Yano. Ultrasound thermometry in hyperthermia. In *Ultrasonics Symposium, 1990. Proceedings., IEEE 1990*, pages 1645–1652 vol.3, Dec 1990.

[28] Christakis A. Damianou, Narendra T. Sanghvi, Francis J. Fry, and Roberto Maass-Moreno. Dependence of ultrasonic attenuation and absorption in dog soft tissues on temperature and thermal dose. *The Journal of the Acoustical Society of America*, 102(1), 1997.

[29] A.E Worthington, J Trachtenberg, and M.D Sherar. Ultrasound properties of human prostate tissue during heating. *Ultrasound in Medicine and Biology*, 28(10):1311 – 1318, 2002.

[30] R L Clarke, N L Bush, and G R Ter Haar. The changes in acoustic attenuation due to in vitro heating. *Ultrasound in Med. and Biol*, 29:127135, 2003.

[31] U Techavipoo, T Varghese, Q Chen, T A Stiles, J A Zagzebski, and G R Frank. Temperature dependence of ultrasonic propagation speed and attenuation in excised canine liver tissue measured using transmitted and reflected pulses. *J. Acoust. Soc. Am.*, 115:2859–2865, 2004.

[32] M. Ribault, J.Y. Chapelon, D. Cathignol, and A. Gelet. Differential attenuation imaging for the characterization of high intensity focused ultrasound lesions. *Ultrasonic Imaging*, 20(3):160–177, 1998.

[33] T. C. Robinson and P. P. Lele. An analysis of lesion development in the brain and in plastics by high-intensity focused ultrasound at low-megahertz frequencies. *The Journal of the Acoustical Society of America*, 51(4B), 1972.

[34] R. M. Arthur, W. L. Straube, J. W. Trobaugh, and E. G. Moros. Non-invasive estimation of hyperthermia temperatures with ultrasound. *International Journal of Hyperthermia*, 21(6):589–600, 2005.

[35] Rubens A. Sigelmann and John M. Reid. Analysis and measurement of ultrasound backscattering from an ensemble of scatterers excited by sine wave bursts. *The Journal of the Acoustical Society of America*, 53(5), 1973.

[36] W.L. Straube and R.Martin Arthur. Theoretical estimation of the temperature dependence of backscattered ultrasonic power for noninvasive thermometry. *Ultrasound in Medicine and Biology*, 20(9):915 – 922, 1994.

[37] R. Martin Arthur, William L. Straube, Jason W. Trobaugh, and Eduardo G. Moros. In vivo change in ultrasonic backscattered energy with temperature in motion-compensated images. *International Journal of Hyperthermia*, 24(5):389–398, 2008.

[38] C Simon, P VanBaren, and E S Ebbini. Two-dimensional temperature estimation using diagnostic ultrasound. 45:989–1000, July 1998.

[39] R Maass-Moreno and C A Damianou. Noninvasive temperature estimation in tissue via ultrasound echo shifts. Part I. Theoretical model. *The Journal of the Acoustical Society of America*, 100:2514–2521, 1996.

[40] D Liu, J Jeong, J Ballard, J Bischof, and E S Ebbini. Real-time Monitoring of Thermal and Mechanical Response to Sub-therapeutic HIFU Beams *In Vivo*. In *Proc. IEEE Ultrason. Symp.*, volume , pages 2254–2257, 2010.

[41] Dalong Liu and E.S. Ebbini. Real-time 2-d temperature imaging using ultrasound. *Biomedical Engineering, IEEE Transactions on*, 57(1):12–16, Jan 2010.

[42] N.R. Miller, J.C. Bamber, and P.M. Meany. Fundamental limitations of noninvasive temperature imaging by means of ultrasound echo strain estimation. *Ultrasound in Medicine and Biology*, 28:1319–1333, 2002.

[43] R. Souchon, G. Bouchoux, E. Maciejko, C. Lafon, D. Cathignol, M. Bertrand, and J.-Y. Chapelon. Monitoring the formation of thermal lesions with heat-induced echo-strain imaging: A feasibility study. *Ultrasound in Medicineand Biology*, 31:251–259, 2005.

[44] T Varghese, J A Zagzebski, Q Chen, U Techavipoo, G Frank, C Johnson, A Wright, and F.T Lee Jr. Ultrasound monitoring of temperature change during radiofrequency ablation: preliminary in-vivo results. *Ultrasound in Med. and Biol*, 28:321 – 329, 2002.

[45] M. Pernot, M. Tanter, J. Bercoff, K. Waters, and M. Fink. Temperature estimation using ultrasonic spatial compounding. *IEEE Trans. Ultrason., Ferroelect., Freq. Contr.*, 51(5):606–615, 2004.

[46] C Simon, P VanBaren, and E S Ebbini. Motion compensation algorithm for noninvasive two-dimensional temperature estimation using diagnostic pulse-echo ultrasound.

[47] M J Daniels and T Varghese. Dynamic frame selection for in vivo ultrasound temperature estimation during radiofrequency ablation. *Phys. Med. Biol.*, 55(16):4735–4753, Aug 2010.

[48] E.S. Ebbini. Noninvasive two-dimensional temperature imaging for guidance of thermal therapy. In *Int. Symp. Biomed. Imaging (ISBI)*, pages 884–887, 2006.

[49] J.G. Proakis, C.M. Rader, F. Ling, C.L. Nikias, M. Moonen, and I.K. Proudler. *Algorithms for Statistical Signal Processing*. Printice-Hall, 2001.

[50] M. Bayat, J. R. Ballard, and E. S. Ebbini. Ultrasound thermography: a new temperature reconstruction model and in-vivo results. In *International Symposium on Therapeutic Ultrasound (ISTU)*, April 2014.

[51] K. R. Nightingale, M. L. Palmeri, R. W. Nightingale, and G. E. Trahey. On the feasibility of remote palpation using acoustic radiation force. *J. Acoust. Soc. Am.*, 110:625–634, July 2001.

[52] F.A. Duck. *Physical Properties of Tissues*. Academic Press, London, 1990.

[53] NCRP. Report no. 113: Exposure criteria for medical diagnostic ultrasound: I. criteria based on thermal mechanics. Technical report, Natioanl Council on Radiation Protectin and Measurements, 1992.

[54] Dalong Liu. *Real-time Imaging of Thermal and Mechanical Tissue Response to Focused Ultrasound*. PhD thesis, University of Minnesota, 2010.

[55] M. Bayat, J. R. Ballard, and E. S. Ebbini. Ultrasound thermography in vivo: A new model for calculation of temperature change in the presence of temperature heterogeneity. In *Ultrasonics Symposium (IUS), 2013 IEEE International*, pages 116–119, July 2013.

[56] A. D. Pierce. *Acoustics: An Introduction to Its Physical Principles and Applications*. American Institute of Physics, 2 edition, 1989.

[57] M. F. Hamilton and D. T. Blackstock, editors. *Nonlinear Acoustics*. Academic Press, 1 edition, 1998.

[58] Alex Alaniz, Faouzi Kallel, Ed Hungerford, and Jonathan Ophir. Variational method for estimating the effects of continuously varying lenses in hifu, sonography, and sonography-based cross-correlation methods. *The Journal of the Acoustical Society of America*, 111(1), 2002.

[59] Lawrence Ziomek. *Fundamentals of Acoustic Field Theory and Space-Time Signal Processing*. CRC Press, 1 edition, December 1994.

[60] Nicole Berline, Ezra Getzler, and Michle Vergne. *Heat Kernels and Dirac Operators*. Grundlehren Text Editions. Springer, 1992.

[61] Harry H. Pennes. Analysis of tissue and arterial blood temperatures in the resting human forearm. *Journal of Applied Physiology*, 1(2):93–122, 1948.

[62] Yaakov Bar-Shalom, X.-R Li, and Thiagalingam Kirubarajan. *Estimation wih applications to tracking and navigation*. Wiley-Interscience, 1 edition, 2001.

[63] Dalong Liu, John R Ballard, Alyona Haritonova, Jeungwan Choi, John Bischof, and Emad S Ebbini. Real-time monitoring of thermal and mechanical tissue response to modulated phased-array hifu beams in vivo. In *11th International Symposium on Therapeutic Ultrasound*, volume 1481, pages 227–232. AIP Publishing, 2012.

[64] Andrew Casper, Dalong Liu, John Ballard, and Emad Ebbini. Real-time implementation of a dual-mode ultrasound array system: *in vivo* results. *IEEE Trans Biomed Eng*, May 2013.

[65] J. C. Dainty, editor. *Current Trends in Optics*. Lasers and Optical Engineering. Academic Press, 1 edition, 1995.

[66] J. Bercoff, M. Tanter, M. Muller, and M. Fink. The role of viscosity in the impulse diffraction field of elastic waves induced by the acoustic radiation force. *Ultrasonics, Ferroelectrics and Frequency Control, IEEE Transactions on*, 51(11):1523–1536, Nov 2004.